ISTANBUL TECHNICAL UNIVERSITY ★ GRADUATE SCHOOL

DESIGN OF ANODE ACTIVE MATERIALS FROM HOT DIP GALVANIZING WASTE FOR LITHIUM ION BATTERIES

M.Sc. THESIS

Orhun OĞUZ

Department of Materials Science and Engineering

Materials Science and Engineering Programme

OCTOBER 2024

ISTANBUL TECHNICAL UNIVERSITY ★ GRADUATE SCHOOL

DESIGN OF ANODE ACTIVE MATERIALS FROM HOT DIP GALVANIZING WASTE FOR LITHIUM ION BATTERIES

M.Sc. THESIS

Orhun OĞUZ
(521211008)

Department of Materials Science and Engineering

Materials Science and Engineering Programme

Thesis Advisor: Assoc.Prof. Dr. Billur Deniz KARAHAN

OCTOBER 2024

ISTANBUL TEKNİK ÜNİVERSİTESİ ★ LİSANSÜSTÜ EĞİTİM ENSTİTÜSÜ

LİTYUM İYON PİLLER İÇİN SICAK DALDIRMA GALVANİZ ATIKLARINDAN ANOT AKTİF MALZEMELERİN TASARIMI

YÜKSEK LİSANS TEZİ

Orhun OĞUZ
(521211008)

Malzeme Bilimi ve Mühendisliği Anabilim Dalı

Malzeme Bilimi ve Mühendisliği Programı

Tez Danışmanı: Doç. Dr. Billur Deniz KARAHAN

EKİM 2024

Orhun OĞUZ, a M.Sc. student of İTU Graduate School student ID 521211008, successfully defended the thesis entitled "DESIGN OF ANODE ACTIVE MATERIALS FROM HOT DIP GALVANIZING WASTE FOR LITHIUM ION BATTERIES", which he prepared after fulfilling the requirements specified in the associated legislations, before the jury whose signatures are below.

Thesis Advisor : **Assoc.Prof. Dr. Billur Deniz KARAHAN** .....
İstanbul Technical University

Jury Members : **Prof. Dr. Özgül KELEŞ** .....
Istanbul Technical University

Dr. Vildan BAYRAM KARAKUŞLU .....
TÜBİTAK Rail Transportation Technologies Institute

Date of Submission : 03 October 2024
Date of Defense : 02 October 2024

To my beloved family,

FOREWORD

I would like to express my deepest gratitude to my advisor, Assoc. Prof. Dr. Billur Deniz KARAHAN, for her guidance and support. Her foresight and brilliance in recognizing the potential in areas often overlooked have been invaluable to this work.

I would also like to extend my heartfelt thanks to Prof. Dr. Özgül KELEŞ for her invaluable contributions. Her pioneering work in the field of energy storage in Turkey is the cornerstone of many studies like this.

I am profoundly grateful to Research Assistant İpek TUNÇ for her invaluable support throughout my study. Her guidance, especially during moments of doubt, was crucial in helping me continue. I would also like to thank Istanbul Technical University for all the opportunities it provided me to carry out this study.

I am also thankful to Muhammad Humza ASHRAF for his help and to Istanbul Medipol University Battery Research Lab, and Regenerative and Restorative Medicine Research Center for characterization.

I would also like to express my gratitude to TÜPRAŞ for supporting my study. I also would like to extend my gratitude to Cem AÇIKSARI, Seniha Bülbül AKTAŞ, Hakan EROĞLU and all my dear colleagues at TÜPRAŞ for their influence and assistance.

Also, I would like to extend my heartfelt gratitude to M. Cihan YILDIRIM, Marmara-Siegener Galvaniz A.Ş. for graciously providing raw materials for this study.

To my dear family, their unwavering support and encouragement have been the driving force behind my academic journey. Lastly, I would also like to thank my beloved friends Cem EŞİGÖK, Ece PAŞA, Ece TUNA, Megi ISALLARI and all my friends. Their friendship and support were invaluable throughout this journey.

October 2024

Orhun OĞUZ
(Metallurgical and Materials Engineer)

TABLE OF CONTENTS

Page

ABBREVIATIONS

BEV : Battery Electric Vehicles
CEI :Cathode Electrolyte Interphase
CNT : Carbon Nanotubes
CV : Cyclic Voltammetry
DMC : Dimethyl Carbonate
EC : Ethylene Carbonate
EIS : Electrochemical Impedance Spectroscopy
EST : Energy Storage Technologies
HDG : Hot Dip Galvanizing
HEV : Hybrid Electric Vehicles
LEDC : Litihum Ethylene Dicarbonate
LIB : Lithium-Ion Battery
LiOR : Lithium Alkoxide
MCMB : Mesocarbon Mesobeads
NMP : N-Methyl pyrrolidone
PEO : Polyethylene Oxide
PVDF : Polyvinylidene Difluoride
RPM : Revolution Per Minute
SEI : Solid Electrolyte Interphase
SEM : Scanning Electron Microscope
TMC : Transition Metal Carbonate
TMO : Transition Metal Oxide
XRD : X-Ray Diffraction
XRF : X-Ray Fluorescence

SYMBOLS

%	: Percentage
°C	: Celsius Degree
λ	: Lambda
Ω	: Ohm
Θ	: Theta
A	: Ampere
Å	: Angstrom
µA	: Microampere
µm	: Micrometer
cm	: Centimeter
e^-	: Electron
eV	: Electronvolt
g	: Gram
h	: Hour
Hz	: Hertz
K	: Kilo
L	: Liter
M	: Molar
mg	: Milligram
mA	: Milliampere
meV	: Millielectronvolt
min	: Minute
mL	: Milliliter
mm	: Millimeter
mM	: Millimolar
mV	: Millivolt
nm	: Nanometer
s	: Second
W	: Watt
V	: Volt

LIST OF TABLES

Page

LIST OF FIGURES

Page

DESIGN OF ANODE ACTIVE MATERIALS FROM HOT DIP GALVANIZING WASTE FOR LITHIUM ION BATTERIES

SUMMARY

The galvanizing process, which is especially important in the automotive industry, entails coating steel or iron with zinc to prevent corrosion. In 2023, the global market for galvanized steel is estimated to be approximately $120 billion, with Turkey leading the MENA region and having a production capacity of about 4 million tons. Common waste types in hot dip galvanizing (HDG) plants include flue dust, (which is formed 30-50 thousand tons annually and contains 50-80% Zn), dross (which is formed 600-800 thousand tons annually and contains 92-97% Zn) and zinc ash (which is formed 500-700 thousand contains 50-70% Zn). Recycling these wastes minimizes economic losses and reduces the environmental impacts of the galvanizing process. Therefore, many studies have been conducted in academia and industry to recycle these wastes and/or recover valuable types of zinc rich compounds from these wastes to contribute to environmental sustainability and adding economic value.

The hypothesis proposed in this thesis is that by using industrial waste as the starting material, it is possible to fabricate low carbon footprint electrode active materials to be used in LIB. This approach focuses on sustainability and environmental friendliness, seeking to create high value-added applications from waste. Knowing that lithium ion batteries (LIBs) are the most common energy storage solutions today, and their performance heavily depends on the quality of the anode active material, their fabrication is reported to increase exponentially in upcoming years following the high demand of consumers. In the current state-of-the-art graphite is widely used as anode active material (AAM) as it delivers 372 mAh/g theoretical capacity. However, China holds a strong position in the graphite market due to abundant mineral reserves. Also, the extraction of graphite is heavily reliant on mining activities. This dependence on limited resources and the significant CO_2 emissions from graphite mining drives the ongoing search for new and more efficient anode materials with higher capacity than graphite.

Therefore, for the first time in the literature, by making appropriate material selection and process design, wastes such as HDG flue dust and HDG dross are obtained from the industry and used as starting material to fabricate Fe-doped ZnO/C composite and $Zn_5(CO_3)_2(OH)_6$ powders, respectively.

The thesis consists of two parts. In the first part, our hypothesis is to obtain Fe-doped ZnO/C composite from the hot dip galvanizing flue dust to fabricate a low carbon footprint anode active material that delivers higher capacities (than that of the graphite: 372 mAh/g) over 100 cycles. In the design of AAM, Fe doping creates electronic conductive pathways to enhance the electrochemical performance of ZnO, while the addition of C improves the overall conductivity, decreases charge transfer resistance and improves the structural stability of the composite with its stress accommodation ability. Knowing that the flue dust is formulated as $Zn(NH_3)_2Cl_2$, it contained 0.8% iron (Fe), 52.18% zinc (Zn) and 45.97% chloride (Cl). Therefore, in the experiments

firstly the flue dust was processed through a neutral leaching process. The aim was to increase the amount of ammonia and chloride in the leachate while maximizing the amount of zinc and iron in the solid residue. By changing one parameter at a time, optimization in temperature, solid-to-liquid ratio, and duration was carried out. The solid residue with the highest Zn and Fe content was attained when neutral leaching was conducted at 80°C, 1:100 solid to liquid ratio, 1 hour, 750 rpm. The Zn amount of the leachate was analyzed by ICP and found to be 320.6 ppm and the chloride amount in the solid residue was analyzed by XRF and found to be 4.12%wt. XRD analysis shows that the solid was mainly composed of zincite (ZnO) and simonkolleite ($Zn_5(OH)_8Cl_2$) compounds. The conditions for transforming $Zn_5(OH)_8Cl_2$ to ZnO were determined through TGA analysis of the leach residue. This leach residue was then heated at 550°C for 4 hours to transform $Zn_5(OH)_8Cl_2$ to ZnO that contained 1.2%wt Fe. Lastly, the Fe-doped ZnO was mechanically processed (milled using a planetary ball mill at 20:1 BPR, 500 rpm for 1 hour) with active carbon in different ZnO/C ratios (1/1 (C1), 2/1 (C2) and 3/1 (C3)), and three different composites were formed. The structural and chemical properties of all powders were characterized. Then, three different electrodes were produced and galvanostatically tested versus Li between 10mV-3V (vs Li/Li^+), under a current load of 50 mA/g in CR2032 coin cells. The results were found to be prominent. The anode (sample C3) prepared with 3/1 ZnO/C ratio delivered 1760.72 mAh/g specific capacity at the first cycle and 592.68 mAh/g specific capacity at the 100^{th} cycle.

In the second part, our hypothesis is that synthesizing $Zn_5(CO_3)_2(OH)_6$ as an AAM from hot dip galvanizing dross will result in a longer cycle life because the AAM chemistry strengthens the SEI at the electrode/electrolyte interface. The design was proposed by taking into account the possible advantages that the carbonated structures of transition metals can provide upon their reactions with Li. It is anticipated that upon discharge, the carbonate in the structure of the material chemistry will strengthen the SEI formation, thus the destructive effects of the high volume change that occurs during the Zn-Li reactions at lower potentials will be controlled and an electrode with a long cycle life will be obtained. Characterization of the dross revealed that this waste generally consisted of 97.87% wt. Zn, 0.5% wt. Fe and 0.8%wt. Cl. To synthesize $Zn_5(CO_3)_2(OH)_6$ from hot dip galvanizing dross, H_2SO_4 leaching was applied with optimized parameters of 0.1M H_2SO_4, 1 hour, and 50°C to achieve 100% leaching efficiency. Following the leaching process, hydrozincite ($Zn_5(CO_3)_2(OH)_6$) was obtained using 0.5M ammonium carbonate ($(NH_4)_2CO_3$) as a precipitating agent under optimized parameters (750 rpm for 4 hours at 80°C, with a 24-hour standing period), achieving a 77.20% chemical precipitation efficiency. This $Zn_5(CO_3)_2(OH)_6$ was then planetary ball milled at 500 rpm, 20:1 ball to powder ratio in 1 hour to reduce agglomerates and decrease the particle size. Finally, an electrode was fabricated and the electrochemical performances of these anodes were galvanostatically tested versus Li between 10mV-3V (vs Li/Li^+), under a current load of 50 mA/g in CR2032 coin cells. This anode delivered 1464.25 mAh/g specific capacity at the first cycle and 222.1 mAh/g specific capacity at the 100^{th} cycle.

The thesis's concept and findings demonstrate that, by using such a novel approach, the thesis not only promotes Turkiye's growth and development objectives but also enriches the intellectual capital in the battery sector and the scientific literature.

LİTYUM İYON PİLLER İÇİN SICAK DALDIRMA GALVANİZ ATIKLARINDAN ANOT AKTİF MALZEMELERİN TASARIMI

ÖZET

Özellikle inşaat ve otomotiv endüstrilerinde büyük öneme sahip olan galvaniz prosesi işlemi, metal yüzeylerin dayanıklılığını artırmak ve korozyonu önlemek amacıyla çelik ya da demir gibi metallerin çinko ile kaplanmasını ifade eder. Bu işlem, metallere ekstra bir koruyucu katman ekleyerek oksidasyon ve paslanma süreçlerini yavaşlatır, bu sayede çelik ve demir yapılar dış etkenlere karşı çok daha uzun süre dayanıklılık gösterir. Galvanizleme işlemi, esas olarak elektrolitik kaplama ve sıcak daldırma olarak iki yöntemle uygulanabilir. Sıcak daldırma yöntemi, çinko kaplama kalınlığı nedeniyle daha kalıcı bir koruma sağlar. 2023 yılı itibarıyla, küresel pazardaki büyüme galvanizli çelik ürünlerine olan talebi artırmış ve bu sektörün toplam pazar değerinin yaklaşık 120 milyar dolar seviyelerine ulaşması beklenmektedir. Türkiye, özellikle Orta Doğu ve Kuzey Afrika bölgesinde lider konumda olup, yılda yaklaşık 4 milyon ton üretim kapasitesine sahip olması sayesinde bu pazarda güçlü bir yer edinmiştir. Sıcak daldırma galvanizleme tesislerinde çeşitli endüstriyel atıklar oluşur ve bunlar arasında baca tozu, cüruf ve çinko külü öne çıkar. Baca tozu, yıllık 30-50 bin ton aralığında üretildiği tahmin edilmekte ve %50-80 oranında çinko içermektedir. Benzer şekilde, cüruf yılda 600-800 bin ton arasında oluşmakta olup %92-97 oranında çinko içerirken, çinko külü ise yılda 500-700 bin ton aralığında oluşmakta olup %50-70 arasında değişen çinko içeriğine sahiptir. Bu atıkların içerdiği yüksek çinko oranları nedeniyle geri kazanımı ekonomik olarak önem arz eder; bu işlemle birlikte çevreye zarar veren atık miktarı da azaltılmış olur. Bu bağlamda, atık yönetimi ve geri kazanım sürecine yönelik akademik araştırmalar ve endüstriyel geliştirmeler yoğunlaşmıştır. Bu geri kazanım yöntemlerinin uygulanması, yalnızca çevresel yükü azaltmakla kalmayıp aynı zamanda ülkenin doğal kaynaklarının korunmasına da katkıda bulunur. Dolayısıyla, galvanizleme tesislerinden kaynaklanan atıkların etkin şekilde yönetilmesi ve bu atıklardan çinko açısından zengin bileşiklerin geri kazanımı, ekonomik değer yaratmanın ötesinde çevresel sürdürülebilirlik açısından stratejik bir önem taşır.

Bu tezde öne sürülen hipotez, endüstriyel atıkları başlangıç malzemesi olarak kullanarak, lityum iyon bataryalarında kullanılacak düşük karbon ayak izli elektrot aktif malzemeleri üretmenin mümkün olduğunu göstermektir. Bu yaklaşım, atıklardan yüksek katma değerli uygulamalar yaratmayı amaçlayarak, sürdürülebilirliğe odaklanır. Lityum iyon pillerin günümüzde en yaygın enerji depolama çözümleri olduğu ve performanslarının büyük ölçüde anot aktif malzemesinin kalitesine bağlı olduğu bilindiğinden, tüketicilerin yüksek talebini takiben önümüzdeki yıllarda üretimlerinin katlanarak artacağı bildirilmektedir. Mevcut durumda grafit, 372 mAsa/g teorik kapasite sağladığı için anot aktif malzemesi olarak yaygın olarak kullanılmaktadır. Fakat Çin Halk Cumhuriyeti'nin bol miktarda grafit rezervine sahip olması nedeniyle pazarda güçlü bir konuma sahip olması, grafitin üretiminin büyük ölçüde madencilik faaliyetlerine bağlı olması ve grafitin yaygın olarak farklı kullanım

alanlarında da tercih ediliyor olması sebebiyle sınırlı kaynaklara olan bağımlılığı azaltıp daha çevre dostu ve yüksek enerji yoğunluğuna sahip alternatif anot aktif malzeme kimyaları üzerine araştırmalar gerçekleşmektedir.

Bu nedenle bu tez kapsamında literatürde ilk kez, uygun malzeme seçimi ve proses tasarımı yapılarak, sektörden temin edilen sıcak daldırma galvaniz baca tozu ve sıcak daldırma galvaniz işlemi cürufu atıkları, sırasıyla demir (Fe) katkılı ZnO/C kompozit ve hidrozinkit ($Zn_5(CO_3)_2(OH)_6$) tozlarının üretiminde hammadde olarak kullanılmıştır.

Bu tez iki bölümden oluşmaktadır. İlk bölümde, hipotezimiz sıcak daldırma galvaniz baca tozundan Fe katkılı ZnO/C kompozitini elde ederek, 100 çevrimde grafitin (372 mAsa/g) üzerinde kapasiteler sağlayan düşük karbon ayak izli anot aktif malzemesi (AAM) üretmektir. Anot aktif malzemenin tasarımında demir (Fe) katkısı, çinko oksitin (ZnO) elektrokimyasal performansını artırmak için elektronik iletken yollar oluştururken, C ilavesi ise genel iletkenliği artırır, yük transfer direncini azaltır ve aynı zamanda da kompozitin yapısal stabilitesini artırır. Baca tozunun yapısının büyük çoğunlukla diamin çinko klorür ($Zn(NH_3)_2Cl_2$) olduğu bilinmektedir ve %0,8 demir (Fe), %52,18 çinko (Zn) ve %45,97 klor (Cl) içerdiği XRF analizi ile belirlenmiştir. Bu nedenle, deneylerde öncelikle baca tozu nötral liç işleminden geçirilmiştir. Amaç, sulu çözeltideki amonyak ve klor miktarını artırmak ve liç katısındaki çinko ve demir miktarını en üst düzeye çıkarmaktır. Liç optimizasyonu deneyleri sırasında bir seferde bir parametre değiştirerek, sıcaklık, katı-sıvı oranı ve süre optimizasyonu gerçekleştirilmiştir. Çinko (Zn) ve demir (Fe) içeriği en yüksek liç katısı, nötral liç işleminin 80°C, 1:100 katı-sıvı oranı, 1 saat, 750 rpm'de gerçekleştirilmesiyle elde edilmiştir. Liç çözeltisindeki çinko (Zn) miktarı ICP ile analiz edilmiş ve 320,6 ppm bulunmuştur. Aynı zamanda liç katısındaki klor miktarı ise XRF ile analiz edilmiş ve ağırlıkça %4,12 olarak bulunmuştur. Nötral liç işlemi sonunda yapılan XRD analizi, katının esas olarak çinko oksit (ZnO) ve simonkolleit ($Zn_5(OH)_8Cl_2$) bileşiklerinden oluştuğunu göstermektedir. $Zn_5(OH)_8Cl_2$'yi çinko oksite (ZnO) dönüştürme koşulları, liç katısının TGA analizi ile belirlenmiştir. Liç katısına, 550°C'de 4 saat ısıl işlem uygulanarak, ağırlıkça %1,2 demir (Fe) içeren ZnO'ya dönüştürülmüştür. Son olarak, elde edilen Fe katkılı ZnO, aktif karbon ile birlikte farklı ZnO/C oranlarında (1/1 (C1), 2/1 (C2) ve 3/1 (C3)) mekanik olarak proses edilerek (gezegen tipi bilyalı değirmen kullanılarak, 20:1 BPR, 500 rpm, 1 saat) üç farklı Fe katkılı ZnO/C kompozit üretilmiştir. Üretilen bütün tozların yapısal, kimyasal ve morfolojik karakterizasyonları yapılmıştır. Ardından, bu tozlar kullanılarak üç farklı elektrot üretilmiştir. Aynı zamanda kompozit öncesi elde edilen demir (Fe) katkılı ZnO tozunun öğütülmüş ve öğütülmemiş hallerinden de elektrotlar üretilmiş ve demir (Fe) katkısının, öğütme etkisinin, kompozit yapının ve farklı ZnO/C oranlarının pil performansına etkisi değerlendirilmiştir. CR2032 düğme pillerde 10mV-3V (vs Li/Li^+) arasında, 50 mA/g akım yükü altında galvanostatik olarak performansları test edilmiştir. Sonuçlar dikkat çekici bulunmuştur. 3/1 ZnO/C oranı ile hazırlanan anot (numune C3), ilk çevrimde 1760,72 mAsa/g spesifik kapasite ve 100. çevrimde 592,68 mAsa/g spesifik kapasite vermiştir.

İkinci bölümde, hipotezimiz, sıcak daldırma galvaniz cürufundan, hidrozinkit ($Zn_5(CO_3)_2(OH)_6$) anodik aktif malzemesi sentezleyerek çevrim testi sırasında elektrot/elektrolit ara yüzeyinde meydana gelen SEI filminin oluşumunu güçlendirerek uzun çevrim ömrüne sahip anot aktif malzeme üretmektir. Tasarım, malzeme kimyası ile birlikte karbonatlı ve hidroksitli yapıların lityum (Li) ile reaksiyonları sırasında sağlayabileceği muhtemel avantajlar dikkate alınarak önerilmiştir. Düşük

potansiyellerde çinko-lityum reaksiyonları sırasında meydana gelen yüksek hacim değişimlerinin olumsuz etkilerinin kontrol edilebileceği ve böylece uzun çevrim ömrüne sahip bir elektrot elde edileceği öngörülmektedir. Cürufun karakterizasyonu, bu atığın ağırlıkça %97,87 çinko (Zn), %0,5 demir (Fe) ve %0,8 klor (Cl) içerdiğini ortaya koymuştur. Sıcak daldırma galvaniz cürufundan hidrozinkit ($Zn_5(CO_3)_2(OH)_6$) sentezlemek için önce, optimize edilmiş parametreler olan, 0,1M sülfürik asit (H_2SO_4) kullanılarak, 750 rpm, 1 saat ve 50°C sıcaklıkta karıştırılarak asidik liç işlemi uygulanmış ve %100 liç verimliliği elde edilmiştir. Liç işlemini takiben, çöktürücü ajan olarak 0,5M amonyum karbonat ($(NH_4)_2CO_3$) kullanılarak hidrozinkit ($Zn_5(CO_3)_2(OH)_6$) elde edilmiştir. Bu işlemin parametrelerinde yapılan optimizasyon sonucunda ise, 80^oC sıcaklıkta, 750 rpm, 4 saat karıştırıldıktan sonra 24 saat bekletilerek, %77,20 kimyasal çöktürme verimi elde edilmiştir. Bu $Zn_5(CO_3)_2(OH)_6$ daha sonra topaklanmayı en aza indirmek ve partikül boyutunu azaltmak için gezegen tipi bilyalı değirmende 500 rpm, 20:1 bilya-toz oranı ile 1 saat öğütülmüştür. Son olarak, elektrot üretilmiş ve bu anotların elektrokimyasal performansları CR2032 düğme pillerde 10mV-3V (vs Li/Li^+) aralığında, 50 mA/g akım yükü altında galvanostatik olarak test edilmiştir. Elde edilen anot malzemesi ilk çevrimde 1464.25 mAsa/g spesifik kapasite ve 100. çevrimde 222,1 mAsa/g spesifik kapasite vermiştir.

1. INTRODUCTION

As the devastating effects of climate change are being experienced, the Paris Agreement was signed in 2016 to limit global warming to +2°C above pre-industrial levels. In line with the Paris Agreement, the European Union prepared the Green Deal, which promotes the use of low-carbon, environmentally friendly, and sustainable materials. In order to fulfill these obligations, efforts are being made to promote the use of renewable energy sources and to reduce the consumption of fossil fuels, particularly through the application of energy storage technologies (EST), the use of which is limited by finite power and energy powers. The solution to this lies in the development of new battery chemistries leading to higher-energy and higher-power densities [1].

The most extensively used rechargeable batteries nowadays are lithium-ion batteries. Significant advances in this discipline have been made since the 1990s. They appear in almost every element of our existence ranging from everyday electrical items to electric cars [2].

Lithium-ion batteries (LIBs) possess significant potential due to their high energy density, long cycle life, and coulombic efficiency. According to 2023 data, 700 GWh of energy is stored worldwide using lithium-ion batteries. This figure is expected to reach 2200 GWh by 2030, 4000 GWh by 2040, and 6000 GWh by 2050. For the production of 1 kWh of energy stored by LIBs, approximately 150 kg of CO_2 emissions are reported. A substantial portion of these emissions, around 20-30%, is attributed to graphite production. Furthermore, the wide range of applications for graphite causes speculation in its price, and most graphite mines are located in China, making it difficult for Europe to meet its long-term sustainable growth targets if graphite is used as an anode active material. Therefore, to achieve sustainable development in battery technology, research on alternative anode chemistries is crucial. The recovery of materials from existing waste and their functionalization as electrode materials stand out as significant research topics in this field [1, 3].

Among alternatives, transition metal oxides attract attention due to their high theoretical capacities since most of them perform conversion reactions with Li [4-6]. At this point, ZnO exhibits a different behavior from other transition metal oxides since it undergoes conversion and then alloying reactions with Li at different states of discharge [7]. Up to now, the use of direct metallic Zn as AAM is not commonly preferred due to the destructive effect of the high volume change exhibited by the Li-Zn reaction. And the low electrical conductivity of ZnO restricts its rate performance as well as its capacity retention capabilities. As a solution, doping, nanoengineering and composite formation of ZnO have been proposed previously [5]. With such motivation, potential investors in batteries are also interested in the market of Zn metal. The global production and consumption of zinc have been steadily increasing, with current consumption levels around 14 million tons annually. A significant portion, approximately 50%, of zinc is consumed in the galvanizing process. However, this process generates substantial waste, notably in the form of dross, ash and flue dust, which poses both economic and environmental challenges [8].

The hot dip galvanizing process occurs by dipping steel substrate into a bath of melted zinc. Depending on the necessary coating thickness and steel surface area, 50–150 kg of zinc is used for coating each ton of steel substrate [9, 10]. Consequently, around 10 kg of dross, 9 kg of ash and 2 kg of flue dust are formed as waste from the hot dip galvanizing (HDG) process of 1 ton of steel substrate [8]. Dross is an important waste product of the hot-dip galvanizing process, generated when iron from the steel reacts with the molten zinc. It is regularly removed from the bath using specialized equipment such as mechanical scoops or dross removal machines. The quantity and composition of dross depend on various factors such as bath temperature, the type of steel being galvanized, and the operational practices in place for dross management [9]. Though zinc oxide makes up the majority of the dross, thirty to forty percent of it is still metallic zinc. Another waste is the ash, which occurs on the surface of the zinc bath as a result of the reaction between molten zinc and oxygen in the air. This reaction produces a light, powdery layer of zinc oxide and other impurities. Zinc ash is regularly skimmed from the surface of the bath to prevent it from adhering to the steel being galvanized. The amount of zinc ash generated is influenced by factors such as bath temperature, exposure to air, and the quality of fluxing [8]. Flue dust is another significant waste of the hot dip galvanizing process, arising from the volatilization of

zinc and other metals during the galvanizing process. It comprises fine sized, oxide rich particulates that capture various metals including zinc and impurities like lead and iron. The formation of the flue dust occurs in the exhaust systems of galvanizing baths and is collected using filtration systems. The flue dust composition varies depending on the specific process conditions and the types of steel being treated [4]. Recycling flue dust not only addresses environmental hazards but also recovers valuable zinc, thereby reducing dependence on primary zinc fabrication by mining. In this thesis, the implementation of effective recycling strategies supports sustainable waste management and resource recovery practices within the galvanizing industry. This aligns with global efforts towards circular economy principles, emphasizing the importance of reusing materials and minimizing waste [5].

2. LITERATURE REVIEW

2.1 Hot Dip Galvanizing

Steel is a vital construction material prized for its strength and versatility. However, its susceptibility to rust, a form of iron oxide, significantly limits its lifespan when exposed to the air. Galvanizing is the process of applying a protective zinc coating onto a steel substrate, offering a robust solution to combat rust and extend the service life of the steel product [11-13].

Galvanizing steel can be achieved through several techniques, each tailored to specific industrial needs and outcomes. Electrogalvanizing involves the application of zinc to steel through electrochemical processes, providing a fine, controlled zinc coat that is ideal for products requiring precise dimensional tolerances and a smooth finish [14]. Sherardizing, or thermal diffusion galvanizing, involves heating steel parts in a closed rotating drum with zinc dust, resulting in a zinc-iron alloy coating that offers durable corrosion protection. This method is particularly effective for small items and complex shapes, ensuring uniform coverage without the use of additional external heat [14]. Another method for applying zinc is thermal spraying, which involves spraying molten or powdered zinc onto prepared steel surfaces with a flame or electric arc. This technique allows for the coating of large structures on-site and can be used to repair damaged or worn areas on previously galvanized materials [15].

Despite the advantages of these methods, hot dip galvanizing (HDG) remains the most popular due to its robustness and cost-effectiveness. It involves submerging steel into molten zinc to create a thicker (up to 200 μm) more protective barrier [16]. This method not only ensures complete coverage, including internal areas and sharp corners but also provides superior corrosion resistance due to the metallurgical bond formed between zinc and the underlying steel. Reports show that the first maintenance period, which is carried out when the steel has rusted by 5%, increases dramatically at a higher thickness of galvanized film due to the improved corrosion resistance. In a rural setting, initial maintenance is required after 50 years for a coating thickness of 40 μm,

and 80 years for a coating thickness of 60 µm [18]. Consequently, hot dip galvanizing is the preferred choice for protecting large structures and components exposed to harsh environmental conditions, balancing long-term durability with economic efficiency [14].

In the practice of HDG, steel is immersed in molten zinc at approximately 450°C, where a chemically bonded layer of zinc and zinc-iron alloys forms at the interface [17]. This coating effectively shields the underlying metal from corrosion and can significantly extend the life of steel structures [11-13]. The durability and reliability of the zinc coating make hot dip galvanizing the preferred choice for protecting steel used in harsh environments, such as outdoor infrastructure, automotive bodies, and marine applications [18, 19].

The process of hot dip galvanizing is renowned not only for the robust protection it offers but also for the comprehensive coverage it achieves. The molten zinc bath ensures complete immersion and coverage of complex shapes, ensuring that every nook and corner of the steel structure is protected [20]. Once the steel is withdrawn from the bath, the zinc solidifies into a dense, impermeable coating that is tightly bonded to the steel, providing both barrier and cathodic protection [21]. Cathodic protection is particularly important as it ensures that, in cases where the coating is damaged, zinc will corrode preferentially to the steel, thereby continuing to protect the steel from corrosion [22, 23].

Over the years, zinc has been used in hot dip galvanizing processes far more frequently. Merely 32% of the world's zinc production was put to use for this in 1960. However, by 2022, 6.8 metric tons, or more than 50% of the world's total zinc production of 13.6 million tons, had been consumed [14, 24, 25].

The largest producers of zinc are known to be China, Australia, and Peru [26]. China has emerged as the largest market for hot dip galvanized steel, with an estimated production of 44 million tons of galvanized steel in 2017. The latter reflects the critical role of hot dip galvanizing in modern manufacturing and construction sectors, where the longevity and safety of metal structures are paramount [11-13].

In addition to its industrial applications, hot dip galvanizing is increasingly recognized for its contributions to sustainable practices. By significantly enhancing the lifespan of steel products, the process reduces the need for frequent replacements of steel,

thereby minimizing waste and conserving the raw materials and energy, typically required for steel production. From an economic perspective, the long-term cost benefits of galvanizing are considerable. The initial investment in galvanizing can prevent future costs associated with corrosion damage and maintenance, making it a cost-effective solution for long-term infrastructure projects [14, 27].

The environmental benefits of hot dip galvanizing also include its ability to be completely recycled without loss of physical or chemical properties, further contributing to its appeal as a sustainable choice. As industries continue to seek environmentally friendly solutions, hot dip galvanizing stands out as a method that not only preserves the structural integrity of steel but also supports broader environmental conservation efforts. By significantly extending the lifespan of steel structures and components, galvanizing contributes to resource conservation and waste reduction. The durability provided by the zinc coating is particularly crucial in harsh environments, reducing the need for frequent maintenance and replacement [14, 15].

Hot dip galvanizing can be either batch-type or continuous. In batch-type galvanizing, individual steel components are cleaned and immersed in molten zinc, making it suitable for larger or uniquely shaped items, such as structural beams or small batches of custom parts [28]. Batch galvanizing provides a thicker, more robust zinc coating, but it is slower and less suited for mass production due to the need for individual handling of each component. On the other hand, continuous galvanizing involves passing steel sheets, wires, or strips through a molten zinc bath in a continuous process, which allows for high-speed coating of materials that are typically thinner, such as sheets used in automotive or construction industries [29]. This method yields a more uniform coating but thinner zinc layers compared to batch galvanizing, making it ideal for large-scale production. Both methods involve similar preparation steps, such as cleaning and fluxing, but differ in application scale and coating thickness. Continuous galvanizing is more widely used in industries requiring mass production, such as in the manufacturing of steel sheets and coils for automobiles and appliances, while batch-type is preferred for smaller quantities or larger, more complex structures [28]. In this study, wastes are used from batch type hot dip galvanizing processes.

The effectiveness of hot dip galvanizing is highly dependent on the cleaning, preparation and processing of the steel. Illustrated in Figure 2.1 as the surface

preparation step, the process begins with crucial surface preparation, where the steel undergoes three main processes which are degreasing, pickling, and fluxing [13].

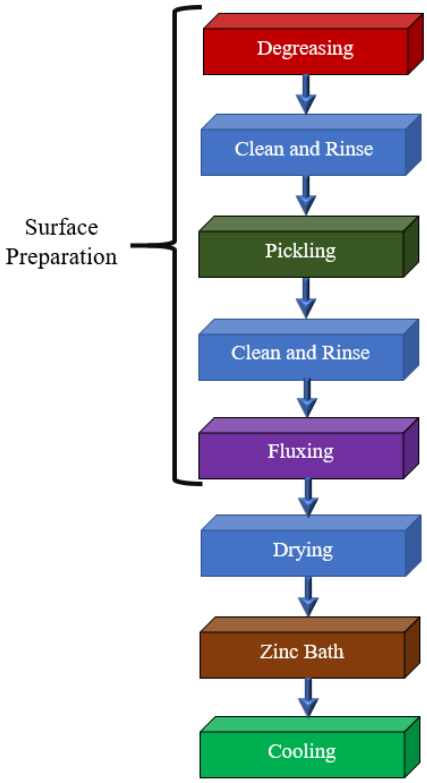

Figure 2.1 : Hot dip galvanizing process flow chart [13].

In degreasing, to remove organic contaminants such as dirt, oil, and grease the substrate is processed into a hot alkaline solution, or a mild acidic solution. Degreasing could be done with or without the current application. The aim is to ensure that the surface is completely free of any substances that could inhibit the adhesion of the zinc coating [30].

Then in pickling, by immersing the substrate in a dilute solution of hydrochloric or sulfuric acid rust and mill scale are removed, clean, naked steel surface is prepared for the next step. The acidic solution selectively reacts with oxides, to effectively clean the steel surface without altering its composition or properties [13, 14].

Finally, in fluxing to ensure optimal adhesion of the zinc coating to the steel substrate, and prevent oxidation before the steel is dipped into molten zinc, the steel substrate is immersed in a flux solution, typically composed of zinc ammonium chloride ($(NH_4)_2ZnCl_4$) (Equation 2.1). Fluxing provides a clean, reactive surface that enhances the bonding of zinc to steel. Fluxing can be performed using either a wet or dry method. In the wet method, the steel is dipped in the flux solution just before being immersed

in the molten zinc, while in the dry method, the steel is dried after fluxing, allowing the flux to remain on the surface as a thin, dry layer [9, 31]. Proper control of the flux composition, temperature, and immersion time is critical, as poor fluxing can lead to defects such as bare spots, rough surfaces, or uneven coating thickness [13, 27, 32, 33].

$$Fe_2O_3 + 3ZnCl_2 \rightarrow 5Zn + 2FeCl_3 + 3ZnO \quad (2.1)$$

Once prepared, steel is submerged in molten zinc, leading to the formation of intermetallic phases at the interface between the steel substrate and the zinc coating. This reaction is primarily diffusion-controlled, resulting in the occurrence of three distinct intermetallic layers typically identified as the gamma (γ), delta (δ), zeta (ζ) phases and one pure zinc layer identified as eta (η) layer. The gamma layer, which is closest to the steel substrate, is rich in iron, while the delta and zeta layers progressively incorporate more zinc. Formation of these layers can be seen in Equations 2.2, 2.3 and 2.4. The growth of these layers depends significantly on the immersion time and temperature during the galvanizing process [34-36]. This layering is not merely superficial and it bonds deeply with the steel to provide lasting protection against corrosion. Finally, the outer eta (η) layer, which is composed almost entirely of pure zinc is soft and ductile, providing the galvanizing coating with its characteristic shiny appearance. This layer is crucial for initial corrosion protection since zinc is more reactive than steel and will preferentially corrode in a corrosive environment, thus protecting the steel underneath. The steel is then slowly withdrawn from the bath, allowing the excess zinc to drain off and form a smooth, clean finish [27].

Gamma (γ) Layer Formation:

$$3Fe + 10Zn \rightarrow Fe_3Zn_{10} \quad (2.2)$$

Delta (δ) Layer Formation:

$$Fe_3Zn_{10} + 11Zn \rightarrow 3FeZn_7 \quad (2.3)$$

Zeta (ζ) Layer Formation:

$$FeZn_7 + 6Zn \rightarrow FeZn_{13} \quad (2.4)$$

2.2 Hot Dip Galvanizing Wastes and Their Recycling

Three main types of waste are produced during the hot dip galvanizing process: flue dust, dross (bottom dross) and ash (surface dross). The locations of these three wastes can be seen in Figure 2.2 [27].

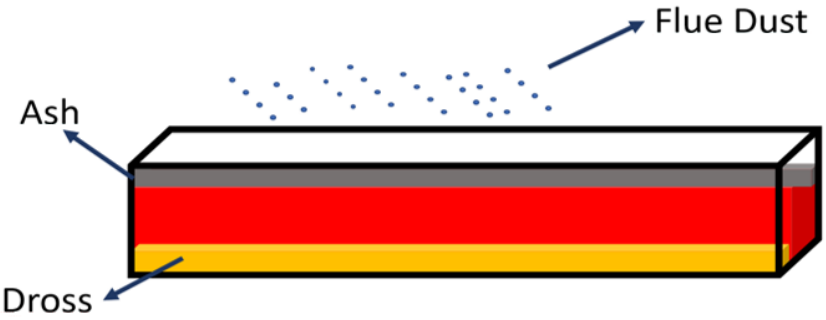

Figure 2.2 : Scheme of hot dip galvanizing process zinc bathing wastes.

2.2.1 Flue dust and its recycling

Both the pre-treatment process and the immersion of steel components in zinc melts produce gaseous wastes. Galvanizing flue dust forms when the fumes cool, and it gets caught in the filters. The flue has a critical position due to its hazardous composition: EPA (Environmental Protection Agency, European Waste Catalog and Hazardous Waste List, KO61) [37]. The flue dust comprises fine particles that contain significant amounts of zinc, chlorine, ammonia and traces amounts of iron, lead, magnesium and aluminum [38]. The management of this dust represents a technical challenge since improper handling can lead to severe pollution issues. Therefore, in order to support the development of the hot dip galvanizing sector and the creation of a sustainable and ecologically friendly environment, increasing the efficacy of flue dust recycling and disposal utilizing the suggested approach is essential [10, 39-45].

The flue dust is basically made of $Zn(NH_3)_2Cl_2$ phase [10]. The main mineral phases identified include $Zn(NH_3)_2Cl_2$, $(NH_4)_2ZnCl_4$, $(NH_4)_2ZnCl_2$, $Zn_5(OH)_8Cl_2{\cdot}H_2O$, and $(NH_3OH)Cl$. The primary source of fume formation is the flux's (zinc chloride and ammonium chloride) decomposition. The flux is essential to use for enhancing the coating adhesion to the substrate. In ideal working conditions, the residue from the flux is needed to be eliminated. However, in practical applications, it is often encountered that the residue of the flux remains on the substrate surface. Therefore, this residue reacts with the molten zinc in the bath and forms $Zn(NH_3)_2Cl_2$ which is a very volatile compound [46-60].

Reviews of the literature reveal that 0.3 kg of flue gas dust is produced during the galvanization of 1 ton of steel [10]. Therefore, Pirošková et al. claim that hydrometallurgical processes offer an effective approach for the selective recovery of zinc from the flue dust, and they suggest a two-step leaching method: including neutral leaching and acid leaching [10]. The flowchart of this process can be seen in Figure 2.3. Herein, neutral leaching separates flue dust to leachate containing zinc chloride based solution and leaching residue containing zinc oxide and impurities with efficiencies ranging from 54.09% to 62.70% [61]. Impurities such as iron, lead and aluminum remain in the leach residue [62]. Leaching residue that contains approximately 40% of the zinc is further leached using acids such as HCl or H_2SO_4, which also dissolve other impurities present in the flue dust [10]. Zinc sulfate or zinc chloride depending on the acid used in the leaching process and with using Na_2CO_3 or $(NH_4)_2CO_3$, zinc carbonate is obtained. Zinc carbonate is calcinated to obtain zinc oxide [10].

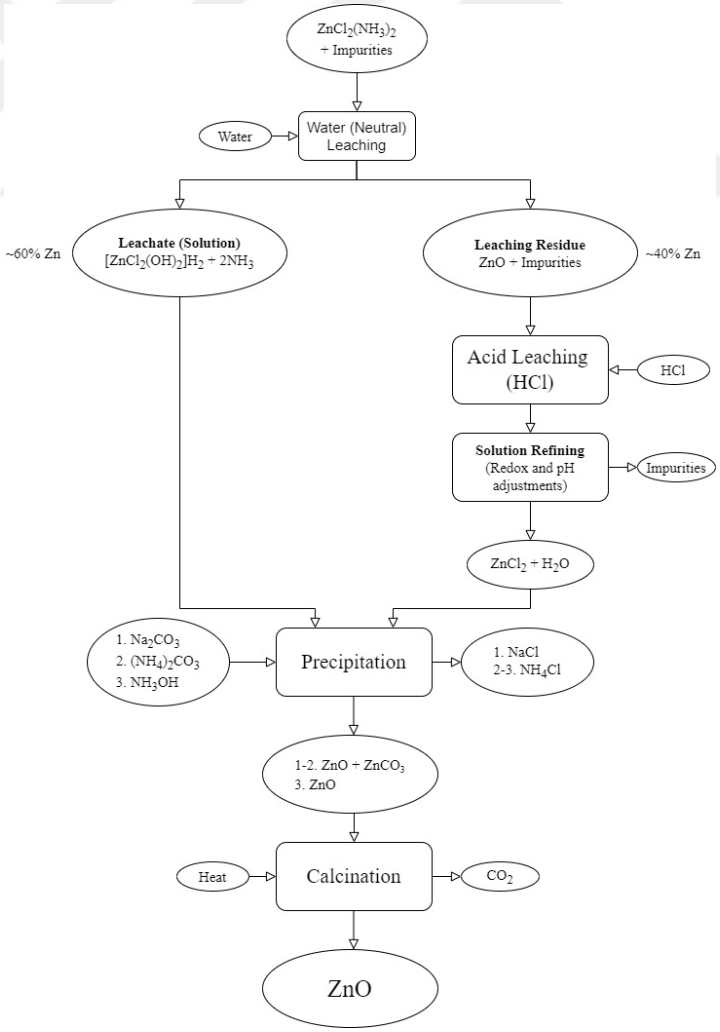

Figure 2.3 : Flowchart of flue dust recycling process [10].

Alternatively, pyrometallurgical processes might be used as they involve the thermal treatment of the flue dust to recover pure zinc ingots (99.2-99.6%) [63]. Unfortunately, these methods leverage high-temperature reactions to separate zinc from other components effectively. While pyrometallurgical methods can achieve high recovery rates, they often require significant energy inputs [63].

2.2.2 Dross and its recycling

Dross is formed when molten zinc reacts with loose iron particles in galvanizing. Knowing that the metallurgical reaction between iron in steel and molten zinc in a kettle is the basis of hot-dip galvanizing, all free iron particles in the kettle tend to react with melted zinc, as expected. There are multiple sources of free iron particles in the galvanizing kettle: i) Iron salts from the steel's interactions with acid salts in the pickling tank and flux from the pre-flux or wet flux layer, ii) the galvanizing kettle itself, iii) the steel being galvanized. As iron has a melting point that is significantly higher than the temperature employed in the galvanizing process and because iron is only 0.035% soluble in zinc at the working temperature of 454°C, the free iron particles in the melted zinc remain in the solid state. Consequently, iron concentrations higher than this proportion will precipitate as particles, which will subsequently react metallurgically with zinc to produce dross. Dross being heavier than molten zinc, the majority of it settles to the bottom of the kettle. Nevertheless, dross floating throughout the kettle can occur by lowering and elevating the steel substrate within the kettle as well as convection currents brought on by temperature variations in the kettle [28].

As zinc is trapped in liquid form during the removal of dross from the zinc bath, it is estimated that around 11% of the total zinc used in the galvanizing process ends up as dross, leading to considerable zinc losses. The high concentration of zinc in this waste implies that recycling dross not only helps to conserve zinc resources but also reduces the environmental impact associated with zinc production [64].

Recent research has focused on optimizing the recovery of zinc from dross. Techniques such as hydrometallurgical processing and pyrometallurgical treatments are being explored to efficiently extract zinc from these byproducts. The goal is to develop sustainable and economically viable methods for zinc recovery, which can help minimize waste and promote the circular economy in the zinc industry [27, 45, 65].

Hydrometallurgical processes for zinc (Zn) or zinc oxide (ZnO) recovery from dross in the hot-dip galvanizing process primarily involve leaching, followed by purification and precipitation stages. Acidic leaching, using sulfuric acid (H_2SO_4), is one of the most common methods, where zinc is selectively dissolved while iron remains in the residue. Alkaline leaching, using solutions like sodium hydroxide (NaOH), sodium carbonate ($NaCO_3$) or ammonium carbonate ($(NH_4)_2CO_3$), offers an alternative approach with higher selectivity for zinc over iron. After leaching, the solution containing zinc ions undergoes purification through techniques such as solvent extraction or ion exchange, where impurities are removed. The purified zinc can then be recovered either as ZnO through precipitation by adding alkali or as pure metallic zinc via electrowinning. In electrowinning, zinc ions are deposited onto cathodes in an electrolytic cell, providing high-purity metallic zinc. Precipitation, on the other hand, yields ZnO, which can be used in various industrial applications. The choice between these methods depends on the desired final product and the economic feasibility of the process. Advances in optimizing leaching conditions, minimizing waste generation, and improving the selectivity of zinc over impurities have significantly enhanced the efficiency of hydrometallurgical recovery of zinc from dross [66, 67].

2.3 Working Principle of Lithium Ion Batteries

Lithium-ion battery (LIB) consists of four essential components which are electrolyte, separator, cathode, and anode as seen in Figure 2.4. The electrolyte serves as a medium that allows ions to move between the anode and cathode during the processes of charging and discharging. This transfer is crucial for the operation of the battery as it enables the transfer of energy. The separator, which is a special type of polymer film, ensures that the anode and cathode do not come into direct contact with each other, otherwise, a short circuit occurs. However, this film is designed to allow lithium ions to pass through its small pores, enabling the battery to function while maintaining safety.

In a lithium-ion battery, charging occurs when electrical energy is supplied to move lithium ions from the positive electrode (cathode) to the negative electrode (anode), where they are stored. Discharging happens when the battery supplies power and lithium ions flow from the anode to the cathode, generating an electric current. In a

half cell configuration, during charging, the anode voltage increases, reaching around 0.1-0.2V relative to lithium metal (Li/Li^+).

In a cell configuration, the cathode, which is the positively charged electrode, is where lithium ions are received during discharge. This process involves a gain of electrons, which is referred to as reduction. On the other hand, the anode is the negatively charged electrode that releases lithium ions during the charging process, a process that involves the loss of electrons, known as oxidation. Throughout the cycle of charging and discharging as seen in Figure 2.5, lithium ions move back and forth between the anode and cathode, embedding themselves in the materials of these electrodes. At the same time, electrons flow through an external circuit, which is what powers devices connected to the battery [68-71].

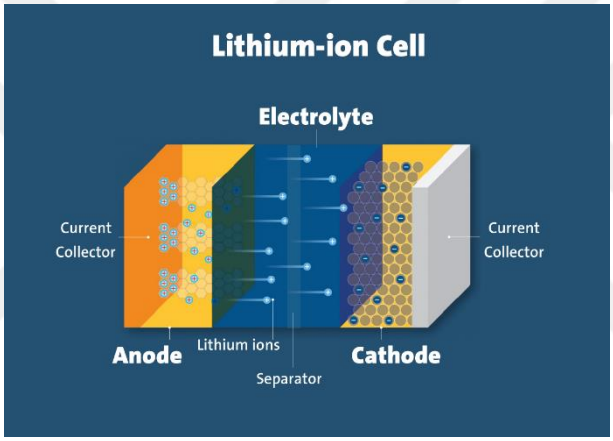

Figure 2.4 : Components of lithium-ion batteries [71].

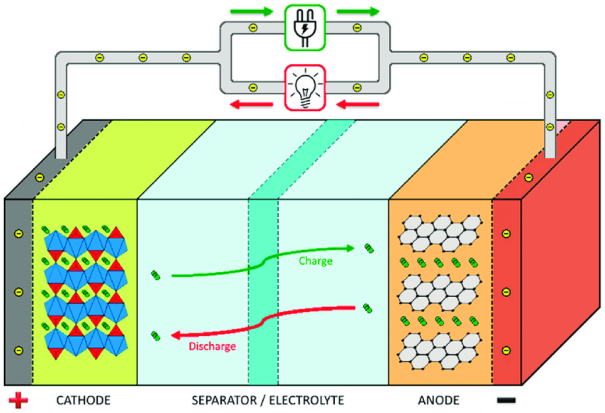

Figure 2.5 : Schematic representation of lithium-ion battery charging and discharging [72].

The ideal cathode (positive electrode) should exhibit reversible reactions with lithium, high electrical and ionic conductivity, and chemical stability against the electrolyte. Additionally, it should be cost-effective, environmentally friendly, and capable of

sustaining long-term cycling stability to ensure the durability and efficiency of the battery. Cathode materials have been developed with various structures, including 1D (olivine), 2D (layered), and 3D (spinel) structures, each offering unique properties that influence battery performance [73, 74].

The negative electrode (anode) is expected to give a reversible reaction with Li^+, accommodating the volumetric expansion in cycling, being economical, safe and environmentally friendly and easy to processability [75]. Three types of reactions can occur at the anode to store and release energy; intercalation, conversion, and alloying/dealloying. During intercalation, lithium ions are reversibly inserted into the crystal lattice of anode materials like graphite without significantly altering the host structure, making it highly stable and efficient. In conversion reaction, materials such as metal oxides undergo a reversible redox process, where lithium ions react with the host material to form new phases, often resulting in higher capacities but with challenges in stability and efficiency. Alloying and dealloying involve the formation of alloys between lithium and metals, silicon is one of the most known materials. These reactions lead to much higher theoretical capacities, but they are accompanied by significant volumetric changes that can cause mechanical degradation over time [76-78].

Electrolyte components in lithium-ion batteries typically consist of a lithium salt for example $LiPF_6$ and a solvent such as ethylene carbonate (EC) or dimethyl carbonate (DMC). Electrolyte salts are expected to offer a high Li^+ transport rate for achieving high power, along with excellent solubility, stability, and non-corrosive properties towards the current collector. Each component has a specific stable operating voltage range that is crucial for battery operation. Electrolyte solvents are expected to have high electrical conductivity, safety and chemical stability [79, 80].

Electrolyte solvents have different stable operating voltages, which depend on the electrode and the electrochemical environment. For example, in a half-cell configuration with a lithium metal reference electrode (Li/Li^+), ethylene carbonate (EC) operates stably within a voltage range of approximately 0.7V to 4.3V, while dimethyl carbonate (DMC) is stable between 1.0V and 4.5V. Depending on the electrode chemistry and whether it's a full-cell or half-cell, the overall battery operating voltage range is determined by the electrochemical stability window of these

electrolytes, which is generally between 3.0V and 4.2V in full-cell lithium-ion batteries [79-82].

At lower voltages, typically below 1.0V vs Li/Li^+ in a half-cell, the electrolyte begins to decompose, leading to the formation of the Solid Electrolyte Interphase (SEI) on the anode. This involves the reduction of electrolyte solvents, such as EC, creating a passivating layer that prevents further decomposition while allowing lithium-ion transport. On the cathode side, at higher voltages above 4.2V vs Li/Li^+, oxidative decomposition of the electrolyte occurs, forming the Cathode Electrolyte Interphase (CEI). Both SEI and CEI are formed due to the decomposition of specific electrolyte components with the applied voltage and stabilize the respective interfaces [81-85].

2.4 Solid Electrolyte Interphase

The Solid Electrolyte Interphase (SEI) is a crucial component in lithium-ion batteries. SEI significantly impacts the performance, safety, and longevity of the batteries. There are four important benefits that SEI provides to a battery which are ionic conductivity, electronic insulation, mechanical stability, and chemical stability. These properties serve the purpose of effectively stabilizing the anode/electrolyte interface, facilitating ion transport at the interface, while contributing to the overall safety and performance of the battery [86, 87].

Lithium ions must be able to pass through the SEI during the charge and discharge cycles, while providing efficient ion transport between the electrolyte and the anode. Therefore ionic conductivity is essential for maintaining the high power and energy densities that make LIBs effective for a wide range of applications [86]. Another important property of the SEI is electronic insulation. The SEI must prevent electrons from passing through it, which helps further electrolyte decomposition after the initial formation of the SEI layer. Moreover, electronic insulation is important for restricting the continuous formation of SEI, because if SEI conducts electrons, SEI can consume active lithium ions and electrolyte, leading to continuous capacity loss with shorter cycle life [88]. Additionally, the mechanical stability of the SEI is crucial. It must be able to withstand the volume changes of the anode material during lithiation and delithiation without cracking or disintegrating. Mechanical strength ensures the SEI remains stable over many cycles, contributing to the long term stability and safety of the batteries [88]. Finally, the chemical stability of the SEI is also very important

because chemical stability provides a protection to the anode by preventing unwanted side reactions that could affect the battery performance. Also, the SEI should ideally have a uniform and defect-free structure. Irregularities or defects in the SEI can lead to localized areas of high resistance or accelerated degradation, adversely affecting the battery's efficiency and lifespan [86, 88].

The formation of the SEI is a complex process that occurs primarily during the initial charge of the battery. Understanding the formation mechanisms of the SEI, especially at the anode, is essential for optimizing battery performance [89].

The SEI forms as a result of the reductive decomposition of the electrolyte at the electrode-electrolyte interface. When a lithium-ion battery is first charged, the electrolyte, which is typically a mixture of organic solvents and lithium salts, begins to decompose at the anode surface due to the potential difference. This decomposition occurs because the reduction potential of many common electrolyte solvents such as ethylene carbonate (EC), dimethyl carbonate (DMC), propylene carbonate (PC) and ethyl methyl carbonate (EMC) is lower than that of lithium, leading to their reduction and subsequent breakdown on the anode surface [86, 89].

Reactions of EC, DMC, DEC, EMC and PC can be seen in Equations 2.5, 2.6, 2.7, 2.8 and 2.9 [89].

$$EC\ (C_3H_4O_3) + 2Li^+ + 2e^- \rightarrow Li_2CO_3 + C_2H_4 \quad (2.5)$$

$$DMC\ (C_3H_6O_3) + Li^+ + e^- \rightarrow CH_3OCO_2Li + CH_4 \quad (2.6)$$

$$DEC\ (C_5H_{10}O_3) + Li^+ + e^- \rightarrow CH_3CH_2OCO_2Li + C_2H_6 \quad (2.7)$$

$$EMC\ (C_4H_8O_3) + Li^+ + e^- \rightarrow CH_3CH_2OCO_2Li + CH_4 \quad (2.8)$$

$$PC\ (C_4H_6O_3) + 2Li^+ + 2e^- \rightarrow Li_2CO_3 + (C_3H_6)_n \quad (2.9)$$

The formation of the SEI can be divided into three steps according to temporal stages which are the reduction of electrolyte components, the growth of reduction products and the deposition of the SEI layer [86, 87].

During the initial stages of charging, when the anode comes into contact with the electrolyte, an electrical double layer, known as the Helmholtz layer, forms at the interface. This layer is characterized by the alignment of solvent molecules and lithium

salt ions at the electrode surface due to the electrostatic attraction between the charged electrode and the electrolyte components. As the potential increases, the ions in the electrolyte begin to move toward the anode, leading to a more pronounced interaction at the surface. Eventually, the electrolyte components, including both the solvent molecules and the lithium salt anions, undergo reduction reactions at the anode surface. The initial reduction typically involves the breaking of chemical bonds in the solvent molecules and the lithium salt, resulting in the formation of various organic and inorganic species. For example, ethylene carbonate and other carbonate-based solvents are commonly reduced to form lithium carbonate (Li_2CO_3), lithium alkyl carbonates, and other byproducts [86].

The reduction products begin to aggregate and grow into a layer on the anode surface. This growth is influenced by the nature of the electrolyte components and the conditions under which the battery is cycled. As the products accumulate, they start to form a more structured layer, initially as a loose aggregation of particles and eventually developing into a more compact and cohesive film. The aggregation process is driven by both the chemical interactions among the reduction products and the physical processes such as diffusion and deposition [86].

The final stage involves the stabilization and maturation of the SEI layer. The SEI typically forms a heterogeneous bilayer structure with an inner inorganic layer including compounds like lithium carbonate (Li_2CO_3) and lithium fluoride (LiF) and an outer organic layer that mainly consists of lithium alkyl carbonates and other organic species. This bilayer structure is crucial as it imparts the dual functionality required of the SEI therefore, it must be ionically conductive to allow lithium ions to pass through during battery operation but electronically insulating to prevent further reduction of the electrolyte [86].

The morphology and composition of the SEI can vary significantly depending on several factors, including the type of anode material, the electrolyte composition, and the cycling conditions. For example, in graphite anodes, the SEI often exhibits a layered structure with a dense inorganic inner layer close to the anode surface and a more porous organic outer layer [86-88].

Another important factor that can improve the performance of the SEI is the electrolyte. Carbonate based electrolytes play a crucial role in the formation and

stabilization of the Solid Electrolyte Interphase (SEI) in lithium-ion batteries (LIBs). Ethylene carbonate (EC) and dimethyl carbonate (DMC) are commonly used for several reasons that contribute to the development of a more durable and effective SEI layer [90].

Carbonate based electrolytes decompose at the anode surface during the initial charging cycles, leading to the formation of a stable SEI layer. For example, in the presence of ethylene carbonate (EC), the decomposition products of carbonate solvents include lithium carbonate (Li_2CO_3), which is a key inorganic component of the SEI. This compound forms a dense and protective layer including lithium ethylene dicarbonate (LEDC), lithium carbonate (Li_2CO_3), polyethylene oxide (PEO) and lithium alkoxide (LiOR) which can be seen in Figure 2.6. This layer prevents further electrolyte decomposition and enhances the overall stability of the SEI [90].

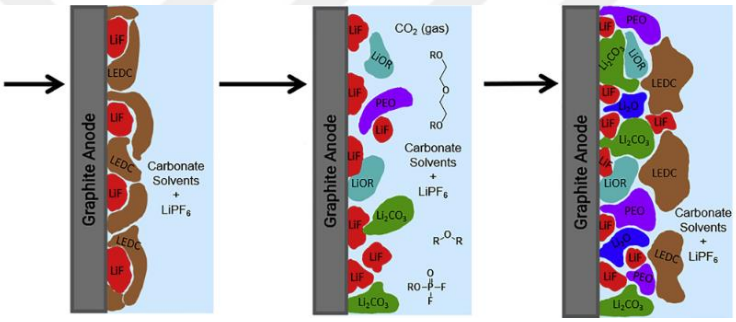

Figure 2.6 : Schematic figure of the SEI formation on the graphite anode [90].

The use of carbonate-based electrolytes results in the formation of an SEI that is chemically stable and resistant to further reactions with the electrolyte. The presence of compounds like lithium hydroxide and lithium alkyl carbonates in the SEI provides a robust barrier against continuous electrolyte breakdown. This stability is crucial for maintaining the SEI's protective properties over many charge-discharge cycles and therefore extending the lifespan of the battery [91].

Carbonate-based electrolytes help form an SEI with good mechanical integrity. The SEI must withstand the volume changes of the anode material during lithiation and delithiation. The inorganic components, such as Li_2CO_3 and LiF, contribute to the mechanical strength of the SEI, preventing cracks and maintaining a continuous protective layer. This mechanical stability is essential for ensuring consistent battery performance and preventing capacity loss [92].

2.5 Lithium Ion Battery Anode Active Materials

Historically, the number of research publications related to lithium-ion battery anodes from 1997 to 2023 is shown in Figure 2.7. Initially, the number of publications was relatively low, with minimal growth observed until around 2009. From 2010 onwards, there has been a significant increase in research, showing a growing interest and investment in lithium-ion battery technology. The notable rise in publications from 2015 to 2020 highlights the rapid advancements and increasing focus on improving battery performance and sustainability, likely driven by the expanding electric vehicle market and the global push for renewable energy solutions. The peak around 2020-2021 suggests a period of intense research, possibly influenced by heightened environmental awareness and technological breakthroughs. Although there is a slight decline in the number of publications in 2022 and 2023, the overall trend demonstrates a significant increase in academic and industrial efforts dedicated to enhancing lithium-ion battery anode materials over the past two decades.

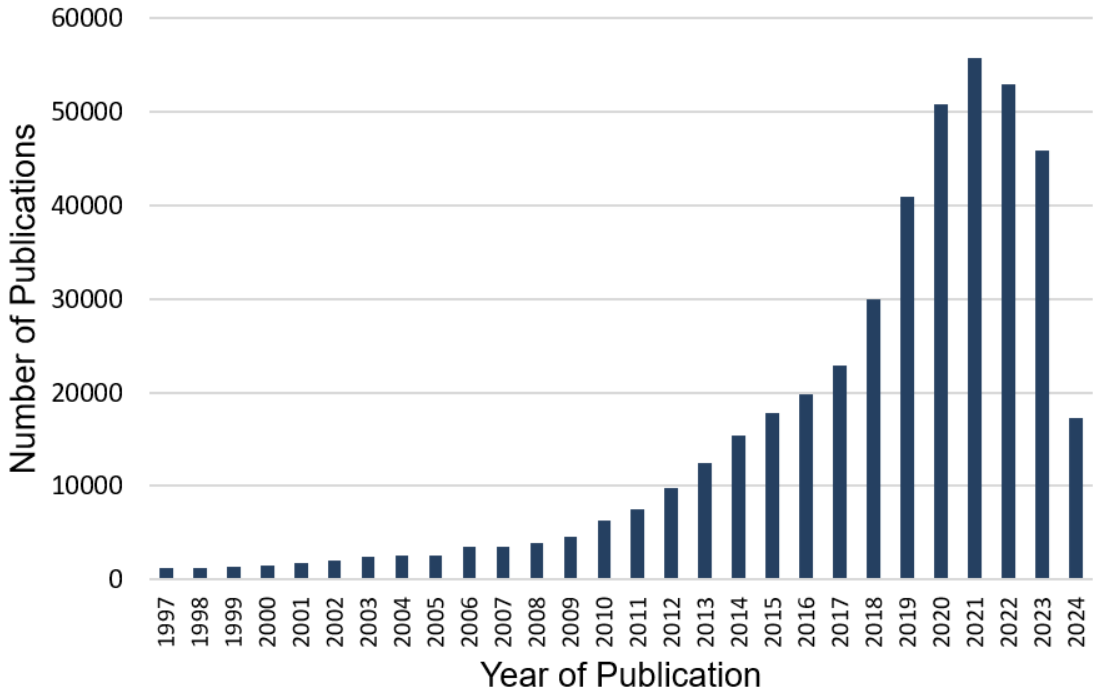

Figure 2.7 : Number of publications on anode material of LIBs from 1997-2024.

Lithium-ion battery anodes can be categorized based on the type of electrochemical reactions they undergo during charge and discharge cycles, namely intercalation, conversion, and alloying reactions, as reported in section 2.3. Understanding the reaction mechanism of the electrode active material is crucial for optimizing anode material's performance and stability in lithium-ion batteries [76-78].

State-of-the-art shows that carbon, particularly graphite, is widely used in commercial cells. Although its capacity is relatively low, its layered structure enables efficient lithium-ion intercalation and deintercalation. However, its structural instability necessitates modification processes like spheroidization and carbon coating. Later, synthetic graphite became a focal point, produced from precursors such as cokes and coal pitches. Synthetic graphites are commercially popular due to their excellent dimensional stability, more negative redox potentials compared to most metal oxides, and high specific charges for Li intercalation [93]. Recently, various terms are used to describe carbonaceous materials for Li-ion batteries, such as soft, hard, and mesophase carbon. Soft and hard carbons are non-graphitic; soft carbons can be graphitized by heating above 2200°C, whereas hard carbons cannot be graphitized even at temperatures as high as 2800°C. Their capacity largely depends on heat treatment. At lower temperatures (<800°C), their specific capacity exceeds 372 $mAhg^{-1}$. Despite high specific capacity values, hard carbons are rarely used in commercial batteries due to poor cycle performance and hysteresis during charge and discharge. Their properties depend significantly on the degree of disorder, which is difficult to control. Soft carbons, after graphitization, offer better electrochemical performance [94]. Alternatively, "mesophase" carbonaceous material, known as mesocarbon microbeads (MCMB), being a liquid-like intermediate phase formed during the heat treatment of soft carbon is studied. Although they offer higher energy densities (300-900 $mAhg^{-1}$) compared to natural and synthetic graphite, microbeads are not widely used due to their cycle life and reversibility. Graphite has higher crystallinity and more ordered layered structures with similar orientations than mesocarbon, making it a more suitable anode material for electric vehicle applications. Therefore, graphite is used in Battery Electric Vehicles (BEVs), while mesocarbon can be used in Hybrid Electric Vehicles (HEVs) for higher capacity needs and also serves as a precursor in graphite production due to its optimal properties [94].

However, to satisfy the demands of consumers recent developments focus on enhancing the capacity of carbon-based anodes through structural and compositional modifications. For instance, the introduction of graphene and carbon nanotubes (CNTs) has been investigated to improve conductivity and capacity, addressing the limitations of natural graphite, such as its relatively low capacity and cycling stability [95].

Another intercalation based anode is the lithium titanate anode. Lithium titanate is recognized for its excellent safety, long cycle life, and zero-strain properties during charging and discharging. Its ability to handle fast charging and discharging makes it suitable for high-power applications. However, its lower capacity compared to silicon and graphite-based anodes limits its energy density. To enhance its performance, researchers are investigating doping and surface modifications [95].

To address the limitations of carbon, researchers have investigated lithium alloys with elements like silicon (Si), tin (Sn), and germanium (Ge). These materials offer higher capacities but face significant volume changes during cycling, leading to mechanical degradation. For example, silicon can theoretically store up to 3579 $mAhg^{-1}$ of lithium, far exceeding the theoretical capacity of the graphite 372 $mAhg^{-1}$, but it expands by up to 300% during lithiation [6]. To mitigate these challenges, strategies such as nanostructuring, using binders, and developing composite materials with more stable elements are being explored. These composites are designed to enhance electrochemical performance by combining the high capacity of silicon with the stability and conductivity of carbon. Advanced fabrication techniques, such as ball milling, thermal pyrolysis, and spray drying, are employed to produce these composites [96]. Ball milling involves mechanically grinding the materials together to achieve a uniform mixture and fine particle size, enhancing the composite's structural integrity and electrochemical properties. Thermal pyrolysis is a process that uses high temperatures to decompose organic materials, resulting in a carbonaceous matrix that improves conductivity. Spray drying is a technique where a liquid mixture of composite materials is atomized into fine droplets and rapidly dried, creating uniform and spherical composite particles [97]. These methods help in achieving a synergistic effect, where the high energy density of silicon is complemented by the mechanical robustness and conductivity of carbon, leading to improved cycle life and overall performance of the anode in lithium-ion batteries. Researchers are continually exploring and optimizing these techniques to develop composite anodes with enhanced capacity, stability, and longevity for next-generation energy storage solutions [96].

Transition metal oxides, such as NiO, Co_3O_4, and ZnO, are being studied for their conversion reaction mechanisms, which offer high capacities. The main advantages of using ZnO as an anode are its environmental friendliness and low cost while providing high output voltage and energy density thanks to its high lithiation and delithiation

potential [10]. On the other hand, using ZnO as an anode causes high volumetric changes in cycling which results in low stability. Moreover, ZnO has low conductivity which restricts its rate performance. Since these disadvantages are not very acceptable as an anode material, modifications are required for nanostructuring ZnO to be used as material [45]. These modifications can be analyzed in three main categories such as structural, compositional and morphological. As a solution different nanostructured ZnO have been fabricated with different morphologies. And to improve the chemical properties, apart from doping with metal ions, composite formation of ZnO with other metal oxides, hybridization of ZnO with carbonaceous materials such as graphene and carbon nanotubes or using metal organic frameworks derived carbons and other derived carbons can be utilized [98].

Also, the main disadvantage of ZnO as an anode material is volume expansion. During the charge and discharge processes, two reactions occur at the anode electrode as seen in Equations 2.10 and 2.11 [99].

Conversion (0.7–1.3 V):

$$ZnO + 2Li^+ + 2e^- \leftrightarrow Zn + Li_2O \quad (2.10)$$

Alloying-Dealloying (0.2–0.7 V):

$$Zn + Li^+ + e^- \leftrightarrow LiZn \quad (2.11)$$

These reactions result in volume expansion and dendrite formation. ZnO anodes, depending on their structure, may have poor conductivity or a non-homogeneous surface that can cause uneven lithium ion distribution. This unevenness promotes localized lithium plating and subsequent dendrite formation. Nanostructured ZnO with the reduced graphene oxide and carbon black modifications which are the most common ways to prevent these types of disadvantages. The volume expansion mechanism can be seen in Figure 2.8 [100].

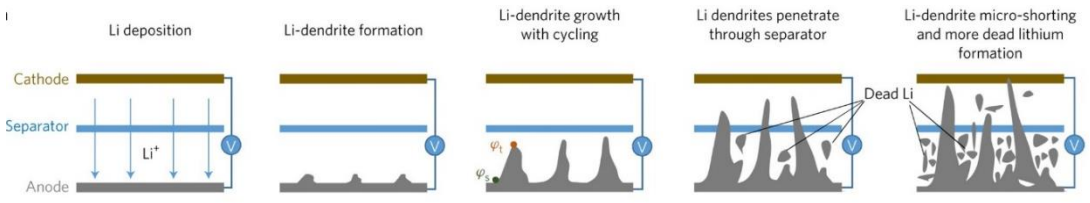

Figure 2.8 : Dendrite formation mechanism in lithium-ion batteries [100].

As reported by Peled et al. [92], carbonate based chemical existence in the cell enhances the SEI's mechanical, chemical and physical properties at the electrode/electrolyte interface, resulting in improved electrochemical performance. Taking this fact as motivation Toyota used Li_2CO_3 directly as anode active material to get high capacity for long cycle life. However the results were not found to be prominent. While using Li_2O_3 as an anode material improved the stability of the SEI layer, it also resulted in poor capacity retention and inefficient cycling stability. Therefore, Wen et al. reported that the composite form of SnO_2-Li_2CO_3/graphite composite anode, benefits carbon's electrical conductivity [101]. Consequently, transition metal carbonates (TMCs) have gained significant attention due to their high lithium storage capacity, intrinsic safety, abundant reserves, and low cost. Historically, TMCs have been primarily used as precursors for synthesizing other transition metal compounds, mainly TMOs. In 2007, Aragón et al. demonstrated the potential of $MnCO_3$ as a LIB anode for the first time, showing significant promise for Li^+ ion storage [102]. Since then, research into the synthesis methods, electrochemical reaction mechanisms, and performance optimization of TMCs has expanded considerably. The key advantages of TMCs as LIB anodes include high theoretical capacities, for example, Zhang et al. reported that porous $ZnCO_3$ anode active material has 735 $mAhg^{-1}$ [103]. This is based on conversion reactions and other electrochemical processes, higher working voltage than graphite anodes thus avoiding lithium dendrite formation and unnecessary side reactions, and cost-effective synthetic methods that enhance production efficiency compared to typical conversion-type anodes of TMOs [104].

Despite these benefits, TMCs face challenges related to slow electrochemical reaction kinetics, poor electronic conductivity, and structural instability due to volume changes during lithiation/delithiation processes. Researchers are working to overcome these limitations through structural modifications and constituent optimization, such as micro-nano structure engineering, heteroatom-doping, multifunctional compositing, and their combinations [105].

Among alternative chemistries, hydrozincite ($Zn_5(CO_3)_2(OH)_6$) having a layered hydroxyl carbonate with a unique structure can facilitate lithium ion intercalation and deintercalation. Also, the presence of hydroxyl groups can improve the electrochemical stability and conductivity of the material.

Han et al. have fabricated hydrozincite synthetically and used it as an anode active material in LIBs [106]. They claim that it has a theoretical capacity of 552 $mAhg^{-1}$ thanks to the multiple oxidation states of zinc which allow more lithium ion accommodations [103]. These benefits also come with challenges. The main challenge for hydrozincite as an anode material for lithium-ion batteries is the same with ZnO anodes which is volume expansion. During lithium insertion and extraction, volume expansion is very high and this results in unpreferable cycling stability. However, hydrozincite's performance can be significantly enhanced by focusing on the formation and stability of the SEI layer.

In literature, Han et al. synthesized ($Zn_5(CO_3)_2(OH)_6$)/graphite composite electrode with hydrothermal method resulting in flaky morphology with a mean thickness of 200 nm results with an initial 746 $mAhg^{-1}$ specific discharge capacity [106]. The electrode performs 299 $mAhg^{-1}$ after 100 cycles [106]. The initial lithiation process involves the reduction of zinc ions and the formation of lithium carbonate (Li_2CO_3) and lithium hydroxide (LiOH), which contribute to the initial capacity. The lithiation/delithitaiton reactions of $Zn_5(CO_3)_2(OH)_6$ is evaluated as in Equations 2.12 and 2.13 [106].

Lithiation-Generation of Li_2CO_3 and LiOH (0.2-0.8 V):

$$Zn_5(CO_3)_2(OH)_6 + 10Li^+ + 10e^- \rightarrow 5Zn + 2Li_2CO_3 + 6LiOH \qquad (2.12)$$

Delithiation-Generation of $ZnCO_3$ and Li—$Zn(OH)_2$ (0.7-1.1 V):

$$5Zn + 2Li_2CO_3 + 6LiOH \rightarrow 5ZnCO_3 + 5Zn(OH)_2 + 10Li^+ + 10e^- \qquad (2.13)$$

Therefore, a powder made of hydrozincite may enable one to benefit the capacity of Zn-Li reaction while providing stable SEI formation by promoting Li_2CO_3 formation at the electrode/electrolyte interface. Because the unique composition of hydrozincite featuring carbonate (CO_3^{-2}) and hydroxide (OH^-) groups, plays a crucial role in the formation and stabilization of the SEI layer. Such a stable SEI layer also reduces impedance growth, providing better mechanical integrity of the electrode against volumetric changes, ion transport hence electrochemical performance.

3. EXPERIMENTAL PROCEDURE

Experimental studies are separated into two main titles which are focused on the hot dip galvanizing (HDG) flue dust and the hot dip galvanizing dross.

3.1 Materials

3.1.1 Hot Dip Galvanizing Flue Dust

The hot dip galvanizing flue dust was provided by Marmara-Siegener Galvaniz A.Ş. can be seen in Figure 3.1. Ethanol is used as a process controlling agent during the planetary ball milling process and commercial grade granulated activated carbon by Norit was utilized for composite formation.

Figure 3.1 : Hot dip galvanizing flue dust.

3.1.2 Hot Dip Galvanizing Dross

The hot dip galvanizing dross was provided by Marmara-Siegener Galvaniz A.Ş. can be seen in Figure 3.2. Hydrochloric acid (H_2SO_4) with %100 purity by Merck was used for preparing a 0.1M leaching solution. Ammonium carbonate ($(NH_4)_2CO_3$), extra pure by Acros Organics was used for preparing a 0.5M chemical precipitation solution.

Figure 3.2 : Hot dip galvanizing dross.

3.2 Processes

3.2.1 Fabrication of Fe doped ZnO/C composite powders from the flue dust

Firstly, neutral leaching of the hot dip galvanizing flue dust, then heat treatment of the leaching residue, then planetary ball milling to reduce the particle size and finally planetary ball milling it with activated carbon was utilized. To discuss the possible use of the ZnO based powder as anode active material in lithium ion batteries, three different composites made of ZnO based powder and activated carbon were ball milled, and three different electrodes were fabricated and tested, respectively. Flowchart to produce Fe doped ZnO/C composite anode active material from the flue dust can be seen in Figure 3.3.

3.2.1.1 Neutral leaching

The flue dust was initially subjected to neutral leaching. In this process, temperature (20^oC-50^oC-80^oC), solid-to-liquid ratio (1:20-1:60-1:100) and duration (30min-60min-90min) were optimized to maximize the ZnO amount in the residue (with minimum Zn^{+2} leaching efficiency). 11 experiments were performed at 750 rpm rotational speed in the IKA C-MAG HS7 magnetic stirrer (see Figure 3.4). The list of parameters for experiments is given in Table 3.1.

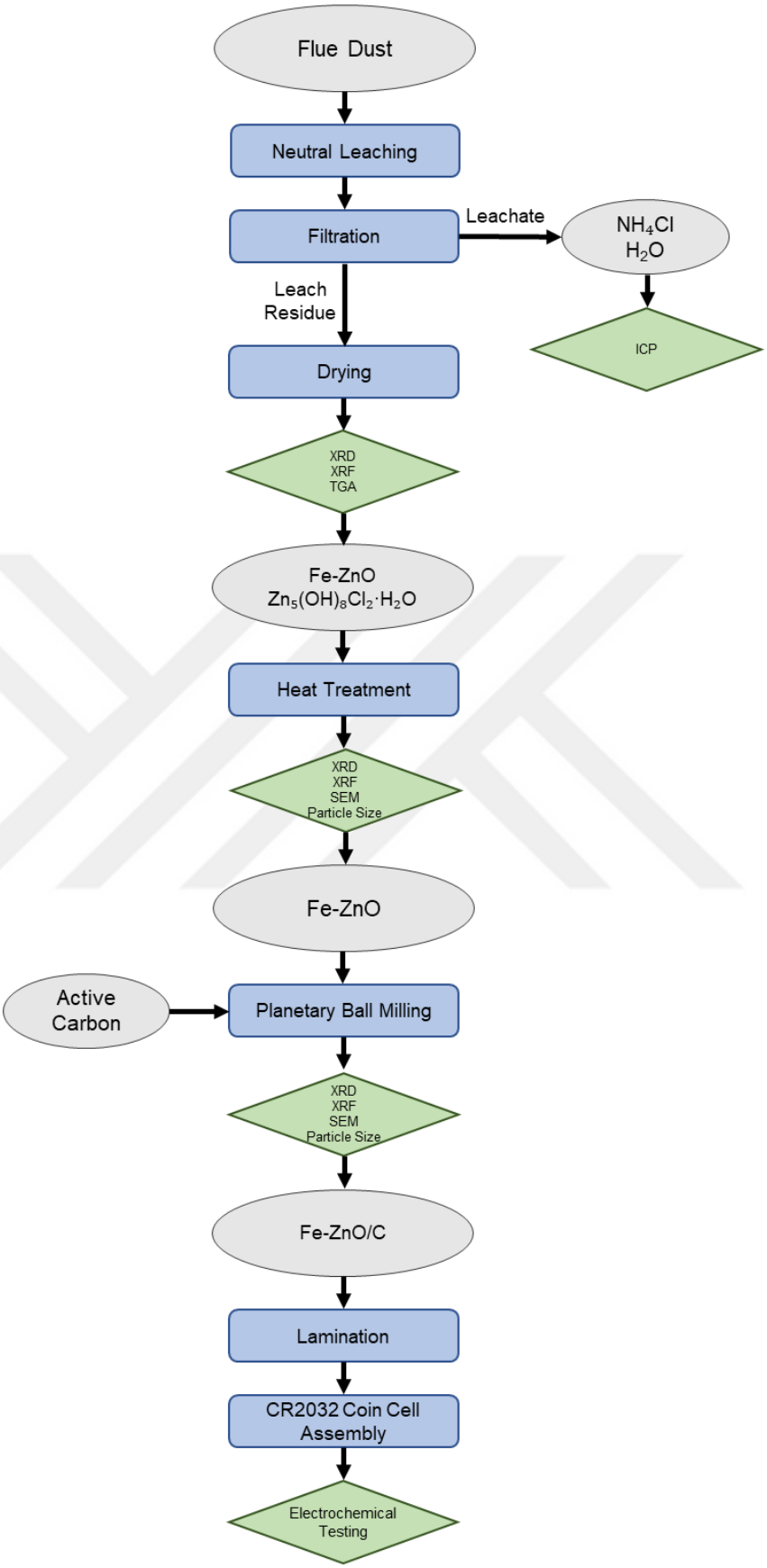

Figure 3.3 : Flowchart to produce Fe doped ZnO/C composite anodes for lithium-ion batteries.

Table 3.1 : Neutral leaching parameters to optimize Zn and Cl amounts in the leach residue.

Sample Code	Solid to Liquid Ratio	Time (min)	Temperature (^oC)	Rotational Speed (rpm)
NL1	1:20	30	20	750
NL2	1:20	30	50	750
NL3	1:20	120	20	750
NL4	1:100	120	20	750
NL5	1:60	120	20	750
NL6	1:60	120	50	750
NL7	1:100	120	50	750
NL8	1:100	30	50	750
NL9	1:100	60	50	750
NL10	1:100	60	80	750
NL11	1:100	30	80	750

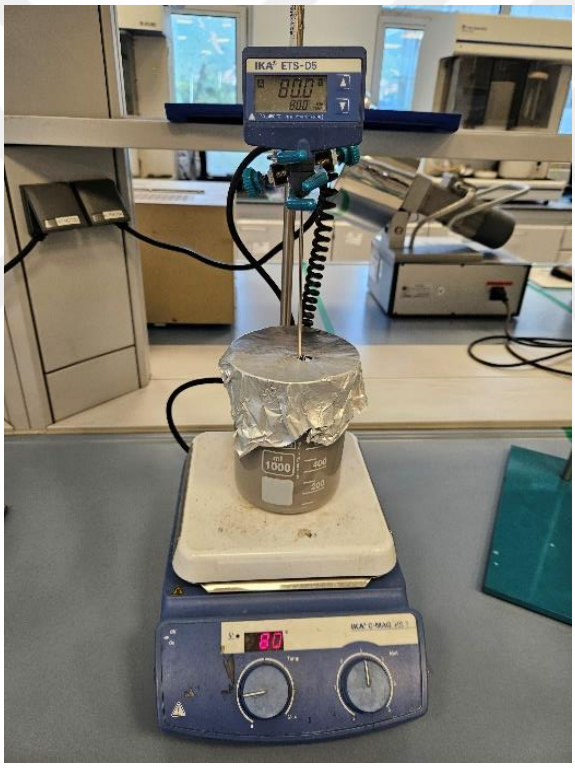

Figure 3.4 : IKA C-MAG HS7 magnetic stirrer.

3.2.1.2 Heat treatment

The Carbolyte AAF 1100 furnace shown in Figure 3.5 was used to perform heat treatment of the leaching residue obtained from the neutral leaching process to form zinc oxide (ZnO). Three different experiments to determine the most efficient heat treatment were carried out at different temperatures (400^{o}C and 500^{o}C) and durations (2 hours and 4 hours).

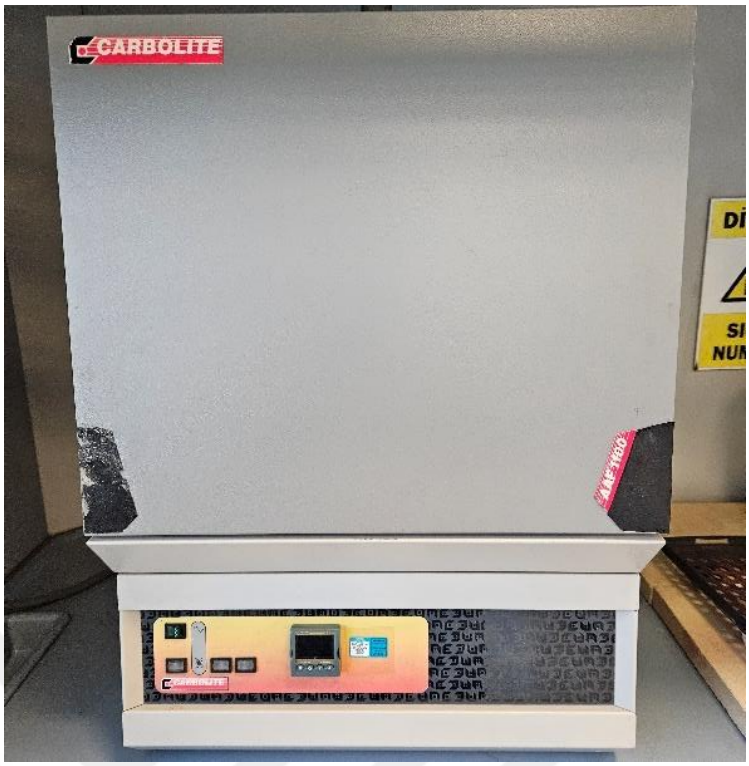

Figure 3.5 : Carbolyte AAF 1100 Furnace.

3.2.1.3 Ball milling

Two step planetary ball milling (Retsch PM 100 with zircon vial) was utilized. At first, planetary ball milling was applied to decrease the particle size of the heat treated leach residue and then to form a composite with activated carbon, another planetary ball milling (see Figure 3.6) was conducted at different parameters. Within the scope, the planetary ball milling of the heat treated leach residue is done using zircon balls (5mm and 10mm in diameter), at 500 rpm, for 60 minutes, with ball to powder ratio of 20:1 and vial filling ratio of 1/3 while adding 50% of particle dispersing agent amount (herein ethanol was selected).

To investigate the influence of composite composition with carbon, planetary ball milling was performed on the heat treated and ball milled leach residue combined with mechanically activated carbon at mass ratios of ZnO/C such as 1/1 (C1), 2/1 (C2), and 3/1 (C3). At first, the active carbon was ball milled in a zircon vial for 30 minutes at 500 rpm, with ball to powder ratio of 40:1 to mechanically activate. Finally, the composite formation is done by introducing the heat treated and planetary ball milled leach residue into the vial containing the mechanically activated carbon. This mixture was processed at 500 rpm with a ball-to-powder ratio of 20:1 for 1 hour.

Figure 3.6 : Retsch PM 100 Planetary Ball Mill.

3.2.2 Fabrication of hydrozincite powders from the dross

In the synthesis of hydrozincite ($Zn_5(CO_3)_2(OH)_6$)powder from the hot dip galvanizing dross, first crushing and sieving, then acid leaching, chemical precipitation and ball milling were applied. To discuss the possible use of hydrozincite ($Zn_5(CO_3)_2(OH)_6$) as anode active material in lithium ion batteries, two different electrodes were fabricated and tested.

3.2.2.1 Crushing and sieving

The hot dip galvanizing dross was crushed using SPEX Sample Prep 800D shown in Figure 3.7 and sieved with 100 μm mesh. This step is necessary to increase the surface are for further processes to be more efficient. Also, the bulk form of the hot dip galvanizing dross is not directly processable with the laboratory equipment.

The flowchart for recycling hot dip galvanizing dross to produce $Zn_5(CO_3)_2(OH)_6$ anodes for lithium-ion batteries can be seen in Figure 3.8.

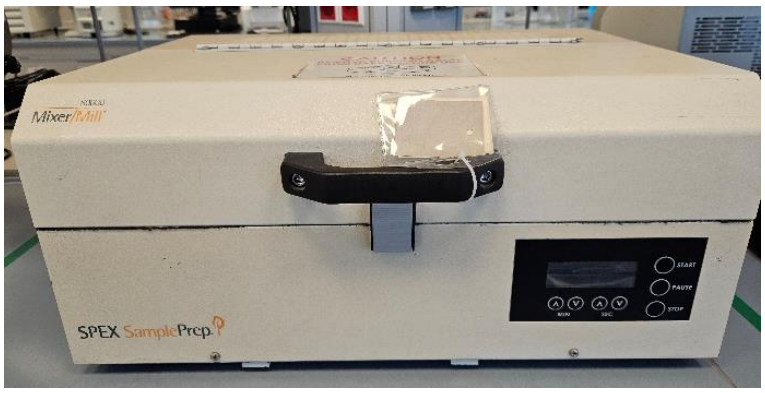

Figure 3.7 : SPEX Sample Prep 800D.

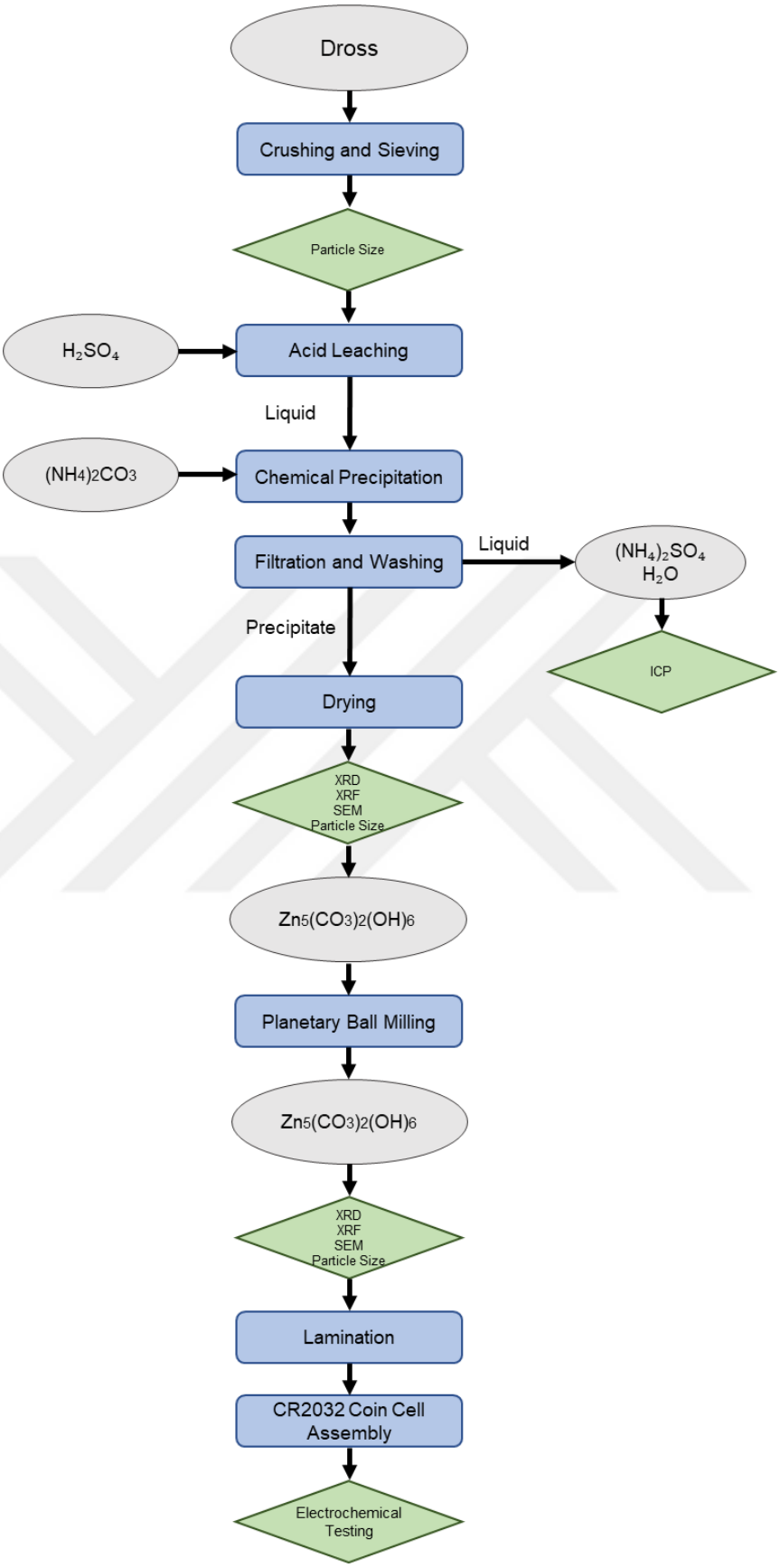

Figure 3.8 : Flowchart for recycling of hot dip galvanizing dross to produce $Zn_5(CO_3)_2(OH)_6$ anode for lithium-ion batteries.

3.2.2.2 Acid leaching

Acid leaching was carried out using H_2SO_4. 0.1M H_2SO_4 is slowly added to the dross at 25°C and 50°C in a 1:1 mole ratio while stirring with a magnetic stirrer at 750 rpm for 1 and 2 hours as shown in Figure 3.9. pH of the reaction is measured as 3.2.

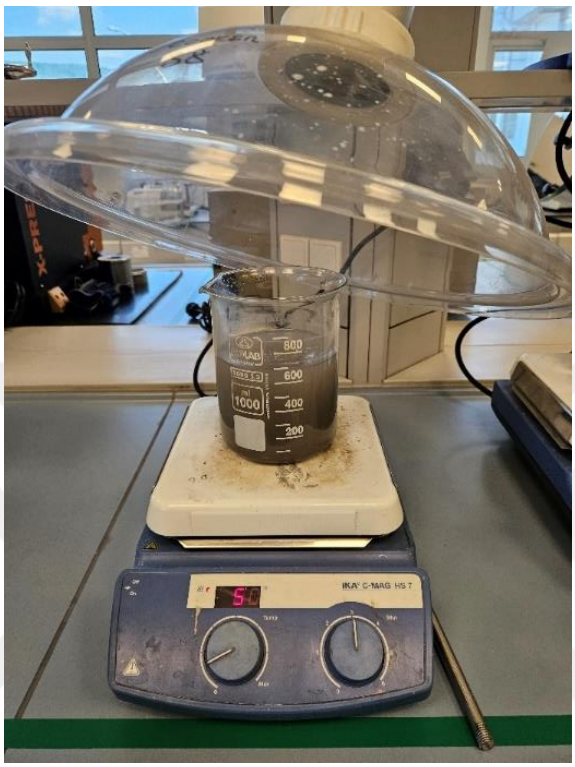

Figure 3.9 : H_2SO_4 leaching experimental setup.

Reactions of this acid leaching are shown in Equations 3.1 and 3.2:

Acid Leaching with H_2SO_4:

$$ZnO + H_2SO_4 \rightarrow ZnSO_4 + H_2O \quad (3.1)$$

$$Zn + H_2SO_4 \rightarrow ZnSO_4 + H_2 \quad (3.2)$$

The conducted experiments are shown in Table 3.2.

Table 3.2 : Parameters for H_2SO_4 leaching.

Sample Code	H_2SO_4 Concentration (M)	Temperature (°C)	Duration (h)	Rotational Speed (rpm)
AL1	0.1	25	1	750
AL2	0.1	25	2	750
AL3	0.1	50	1	750
AL4	0.1	50	2	750

3.2.2.3 Chemical precipitation

Chemical precipitation was carried out using $(NH_4)_2CO_3$. To obtain a slower reaction rate, 0.5M $(NH_4)_2CO_3$ was used. $(NH_4)_2CO_3$ was slowly added to the leachate while mixing with a magnetic stirrer at room temperature at 750 rpm and reached the pH of 6.2 and later filtered as shown in Figure 3.10. To systematically investigate the influence of key parameters on the efficiency of chemical precipitation, seven experiments were conducted. The variables included temperature (25, 50, and 80°C), mixing duration (1 and 4 hours), and an additional waiting period of 24 hours after mixing. In each experiment, only one parameter was varied while keeping others constant, allowing for an isolated analysis of the effect of each factor on the precipitation process. The rotational speed was maintained at 750 rpm across all experiments, and the concentration of $(NH_4)_2CO_3$ was fixed at 0.5 M as seen in Table 3.3. The chemical precipitation reaction is shown in Equations 3.3.

Chemical Precipitation with $(NH_4)_2CO_3$:

$$5ZnSO_4 + 5(NH_4)_2CO_3 + 3H_2O \rightarrow Zn_5(CO_3)_2(OH)_6 + 5(NH_4)_2SO_4 + 3CO_2 \quad (3.3)$$

Table 3.3 : Parameters for chemical precipitation

Sample Code	$(NH_4)_2CO_3$ Concentration (M)	Temperature (^oC)	Mixing Duration (h)	Rotational Speed (rpm)	Waiting Duration (h)
CP1	0.5	25	1	750	-
CP2	0.5	50	1	750	-
CP3	0.5	25	1	750	24
CP4	0.5	50	1	750	24
CP5	0.5	50	4	750	24
CP6	0.5	80	1	750	24
CP7	0.5	80	4	750	24

Figure 3.10 : Chemical precipitation with 0.5M $(NH_4)_2CO_3$ and filtration.

3.2.2.4 Planetary ball milling

The obtained powder was planetary ball milled using Retsch Pm 100. Ball milling was applied at 1 hour at 500 rpm and a 20:1 ball-to-powder ratio.

3.2.3 Electrode preparation and cell assembly

Anode slurries were prepared by mixing the anode active material, conductive agent (Carbon black), and binder (PVDF: Polivinilidin florür) in an organic solvent (NMP: N-Methyl-2-pyrrolidone by Merck) with respect to 8:1:1 weight ratio. Thinky ARE-250 was used for mixing slurry as shown in Figure 3.11. Mixing was conducted three times at 2000 rpm for 120 seconds.

Figure 3.11 : Thinky ARE-250 for mixing the anode mixture.

For the lamination, the prepared anode slurry was poured on a copper foil and using Gelon Group Film Coater GN-HCM-1525 Doctor Blade shown in Figure 3.12, copper foil was coated with the anode slurry at a homogenous thickness of 50 μm.

Figure 3.12 : Gelon Group Film Coater GN-HCM-1525 Doctor Blade.

Then, the coating was dried, rolled to 30 μm thickness with the roll shown in Figure 3.13; then punched for coin cell assembly.

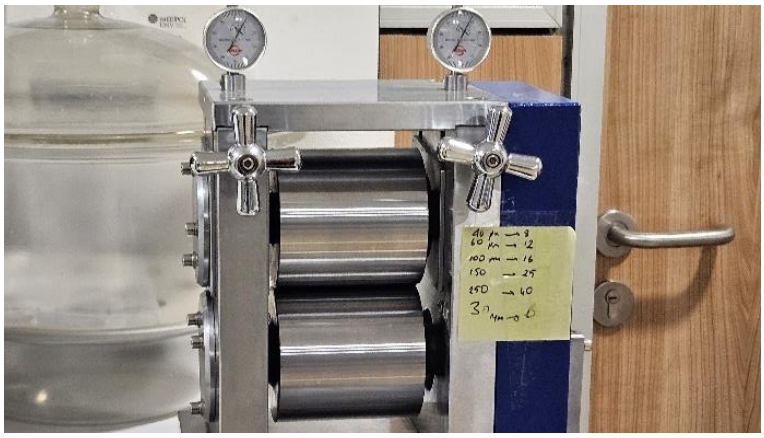

Figure 3.13 : Roll for rolling the electrode on copper foil to 30 μm thickness.

For the electrochemical tests, CR2032 (MTI Corp.) type coin cells are assembled in an argon filled glove box (MBRAUN, Labmaster Pro) having oxygen and humidity levels below 0.1 ppm which can be seen in Figure 3.14. The typical half-cell comprises anode (12mm diameter) punched from coated copper foil, a polypropylene separator (Celgard 2400), lithium cathode (battery grade) and an electrolyte made of 1M lithium hexafluorophosphate ($LiPF_6$) solution in 1:1 ethylene carbonate (EC), and dimethyl carbonate (DMC) (Dongguan Shanshan Battery Materials Co. Ltd., Merck-1.00028.1000).

Figure 3.14 : MBRAUN LABMaster glove box.

3.3 Characterization

3.3.1 Powder characterization

To examine the structural phases, an X-ray diffractometer (XRD, Bruker D8 Advanced Family) was used, scanning from $2\theta = 10^{o}$-80^{o} with a Cu Kα source at a scanning rate of 0.02^{o} per second. Rietveld analysis was applied by mixing the powders with completely crystalline 20%wt. corundum (α-Al_2O_3 by Sigma-Aldrich) to accurately determine the quantitative amounts of all phases using Topas 6.0 software. The morphology of the samples was investigated using a scanning electron microscope (SEM, Zeiss Gemini 500). The chemical composition of the synthesized powder was analyzed using X-ray fluorescence (XRF, Bruker S8 Tiger Series 2). The particle size was determined with the Malvern Analytical Zetasizer Advance Range. Thermogravimetric results were determined with TGA (Perkin Elmer TGA 4000). Solution composition (chlorine and zinc amount) was determined with inductively coupled plasma optical emission spectroscopy (ICP-OES, Perkin Elmer Optima 8000). Energy band gaps were analyzed and calculated with ultraviolet visible spectroscopy (UV-Vis, Perkin Elmer Lambda 25).

3.3.2 Electrode characterization

For the electrochemical evaluation, electrodes are tested galvanostatically between 10mV-3V (vs Li/Li^{+}) under a current load of 50 mA/g by a Neware battery analyzer system seen in Figure 3.15.a. Cyclic voltammetry (CV) test is applied at a scan rate of 0.1 Vs^{-1} between cut-off voltages of 10mV-3V (vs Li/Li^{+}) with using Gamry Interface 100E setup seen in Figure 3.15.b [107].

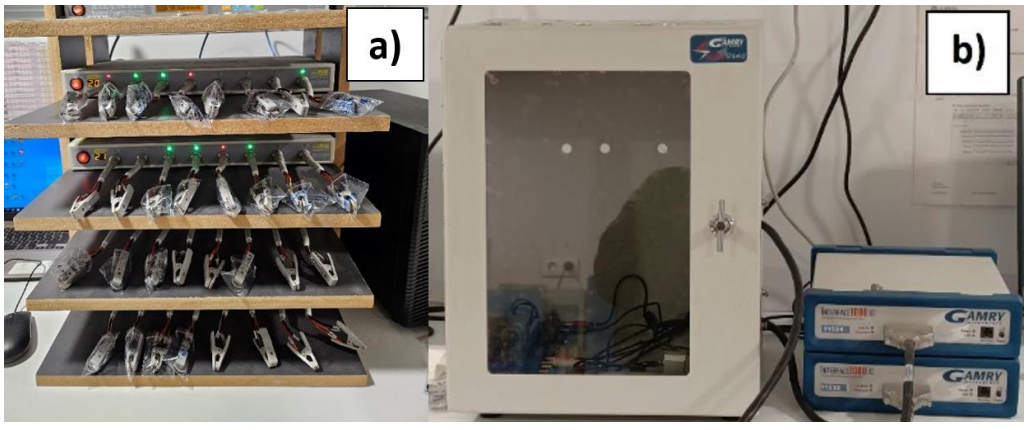

Figure 3.15 : a) Battery analyzer b) Gamry Interface 1000E setup.

4. RESULTS AND DISCUSSION

In the first part of this thesis, Fe doped ZnO/C composite was produced from the recycling of hot dip galvanizing waste flue dust. In the second part of the thesis, $Zn_5(CO_3)_2(OH)_6$ powder was produced from the hot dip galvanizing waste dross. Once the morphological, chemical and structural characterization results of the powders were studied, the possible use of these powders as anode active material in lithium ion batteries was discussed based on the electrochemical performances.

4.1 Design of Fe Doped ZnO/C Anodes from Hot Dip Galvanizing Flue Dust

4.1.1 Characterization of the flue fust

XRF and XRD analyses were applied to characterize the hot dip galvanizing flue dust. XRF results show that the hot dip galvanizing flue dust mainly consists of zinc (Zn 52.28%) and chlorine (Cl 45.97%) making up 98.25% of its weight. It also includes iron (Fe 0.88%) as a minor element. XRF results are given in Table 4.1.

XRD results indicate that the structure of the flue dust consists of mainly $ZnCl_2(NH_3)_2$ and $(NH_4)_2ZnCl_2$ phases which are two similar phases where Zn makes four bonds with chloride and ammonium groups. and XRD results are reported in Figure 4.1. According to Rietveld analysis results, hot dip galvanizing flue dust includes 64.51%wt. of $Zn(NH_3)_2Cl_2$ and 7.94%wt. of $(NH4)_2ZnCl_2$ while including 27.56% amorphous content with goodness of faith (GoF) as 2.23. Fe amount detected in XRF is considered to be an impurity. Therefore, we do not see any peak related to the Fe of the flue dust.

Further processes that the hot dip galvanizing flue dust will undergo will focus on keeping zinc (Zn) and iron (Fe) in the final material while getting rid of the chloride (Cl) since the presence of chlorine in anode active materials can negatively impact battery performance and lifespan, as it often leads to unwanted side reactions, which can increase the possibility of electrolyte decomposition and reduce overall battery stability.

Table 4.1 : XRF elemental analysis results of flue dust.

(%wt.)	Zn	Cl	Fe	Ca	Al	Mn	Si	Others
Flue Dust	52.28	45.97	0.88	0.30	0.29	0.11	0.10	0.07

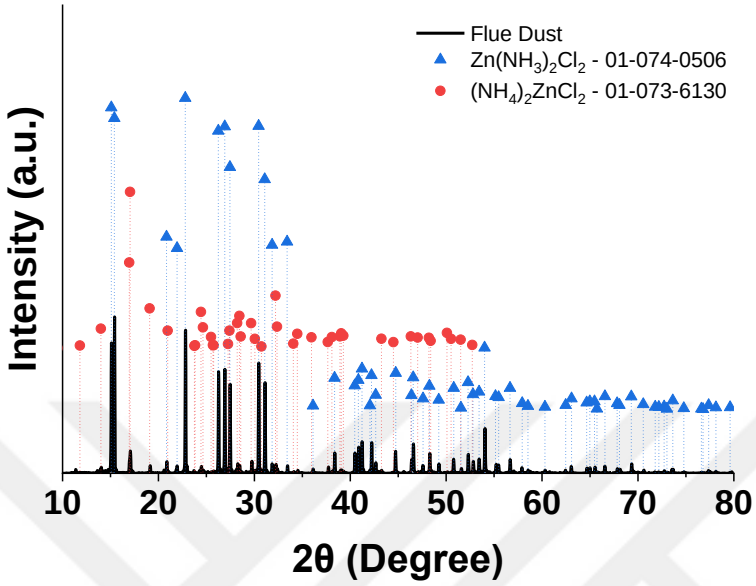

Figure 4.1 : XRD results of hot dip galvanizing flue dust.

4.1.2 Optimization of neutral leaching parameters

Pirošková et al. report that ZnO can be obtained from the hot dip galvanizing (HDG) flue dust starting with the neutral leaching process. Their study focuses on obtaining zinc (Zn) and zinc oxide (ZnO) from hot dip galvanizing flue dust where the neutral leaching occurred at a 1:2 solid to liquid ratio. This process achieves a leaching efficiency ranging from 54.09% to 62.70%, revealing that Zn is present in the leaching residue as ZnO and in the leachate as $ZnCl_2$. They also discover that impurities such as Fe and Al remain in the leaching residue alongside ZnO and other impurities such as Cl in the leachate [10].

In this study, unlike the previous one, it is aimed to obtain Fe doped ZnO (without chlorine) by means of neutral leaching of the HDG flue dust. Therefore, neutral leaching parameters are optimized by taking the Cl amount in the leach residue as a reference, since Cl is necessary to be removed from the system. By increasing the water amount by decreasing the solid to liquid ratio significantly and increasing the temperature while stirring for an optimized duration, ZnO formation is encouraged. These reactions occurring during neutral leaching are shown in Equations 4.1, 4.2, 4.3, 4.4 and 4.5 [10]:

Dissolution:

$$Zn(NH_3)_2Cl_2 \rightarrow Zn^{2+} + 2NH_3 + 2Cl^- \quad (4.1)$$

Ammonia hydrolysis:

$$NH_3 + H_2O \rightarrow NH_4^+ + OH^- \quad (4.2)$$

$Zn(OH)_2$ formation:

$$Zn^{2+} + 2OH^- \rightarrow Zn(OH)_2 \quad (4.3)$$

ZnO formation:

$$Zn(OH)_2 \rightarrow ZnO + H_2O \quad (4.4)$$

Simonkolleite formation:

$$5Zn^{2+} + 8OH^- + 2Cl^- + H_2O \rightarrow Zn_5(OH)_8Cl_2 \cdot H_2O \quad (4.5)$$

Table 4.2 : Optimization of neutral leaching parameters to reduce the Cl amount and maximize the Zn and Fe amounts in the residue: XRF results.

Sample Code	Solid to Liquid Ratio	Time (min)	Temperature (^oC)	Rotational Speed (rpm)	Zn%	Cl%	Fe%
NL1	1:20	30	20	750	65.12	30.16	0.98
NL2	1:20	30	50	750	86.48	9.66	1.20
NL3	1:20	120	20	750	73.56	24.68	1.06
NL4	1:100	120	20	750	87.44	10.22	1.32
NL5	1:60	120	20	750	77.84	19.21	1.11
NL6	1:60	120	50	750	85.38	9.87	1.28
NL7	1:100	120	50	750	89.23	7.88	1.35
NL8	1:100	30	50	750	89.05	8.66	1.40
NL9	1:100	60	50	750	89.20	7.89	1.33
NL10	1:100	60	80	750	93.80	4.12	1.59
NL11	1:100	30	80	750	89.99	6.28	1.43

Table 4.2 presents the results of optimizing neutral leaching parameters to reduce chlorine (Cl) content while maximizing zinc (Zn) and iron (Fe) content in the leachate. The parameters related to the solid-to-liquid ratio, time, temperature, and rotational speed are optimized by changing one parameter at once. The objective is to identify the optimal conditions that yield the highest Zn and Fe content with the lowest Cl

content. The solid to liquid ratios tested are 1:20, 1:60, and 1:100. The results indicate that lower ratios, such as 1:20, generally resulted in lower Zn content and higher Cl content. The times tested are 30, 60, and 120 minutes. Longer leaching times such as 120 minutes do not necessarily improve the Zn content significantly compared to shorter times. Optimal Zn content is achieved at 60 minutes. Moreover, when the effect of temperature (20°C, 50°C, and 80°C) is investigated, higher temperatures were found to significantly reduce Cl content while increasing Zn content, with the highest Zn content observed at 80°C. The rotational speed is constant at 750 rpm for all samples, so its direct impact on leaching efficiency cannot be isolated from this data. Shorter times at high temperatures also provide substantial improvements, suggesting that time can be optimized further depending on industrial constraints.

The results at Table 4.2 indicate that the optimal conditions for neutral leaching to maximize Zn and Fe content while minimizing Cl content are solid-to-liquid ratio of 1:100, a temperature of 80°C, and a leaching time of 60 minutes as in sample NL10. This set of conditions results in the highest Zn content (93.80%) and the lowest Cl content (4.12%), demonstrating the importance of temperature and solid-to-liquid ratio in the leaching process. The repeatability and reliability of these data were confirmed by conducting three additional experiments under the same parameters, yielding Zn contents between 93.67% and 93.98% (standard deviation of 0.11%), and Cl contents between 4.06% and 4.14% (standard deviation of 0.08%). Also, the ICP results indicated that 320.6 ppm of zinc remained in the leach solution, suggesting that most of the zinc was retained in the leach residue, which will undergo further treatment. Figure 4.2 shows the NL10 powder obtained from this neutral leaching process.

XRD result of the sample NL10 also shows that the sample contains two different phases; zincite (ZnO) and simonkolleite ($Zn_5(OH)_8Cl_2 \cdot H_2O$) as seen in Figure 4.3. This shows that the remaining 4.12%wt. Cl exists in the simonkolleite ($Zn_5(OH)_8Cl_2 \cdot H_2O$) phase. Rietveld analysis, with 3.05 goodness of faith (GoF), showed that the sample NL10 consists of 51.11% ZnO, 9.41% $Zn_5(OH)_8Cl_2 \cdot H_2O$ with 39.48% amorphous content. Therefore, further treatments will focus on purifying the material from the remaining chloride by getting rid of the simonkolleite ($Zn_5(OH)_8Cl_2 \cdot H_2O$) phase.

Figure 4.2 : NL10 sample

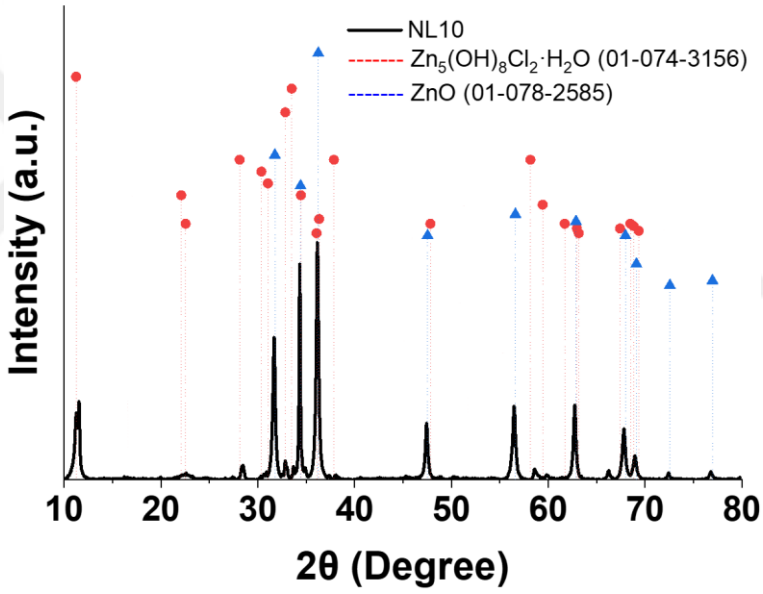

Figure 4.3 : XRD results of NL10 sample

4.1.3 Heat treatment

TGA analysis of the residue (NL10) is given in Figure 4.4. According to the TGA results, the sample loses 5% of its weight by the time it reaches 140^{o}C which can be explained as the evaporation of remaining moisture content. The decomposition of the simonkolleite compound is determined at 400^{o}C. Li et al. have also reported that the simonkolleite phase transforms into ZnO when it is heat treated at 600^{o}C for 3 hours [108]. Thus the heat treatment is applied at 400^{o}C and 500^{o}C and according to the results, 500^{o}C and 4 hours are selected after the optimization of temperature and duration and applied to residue (see Table 4.3).

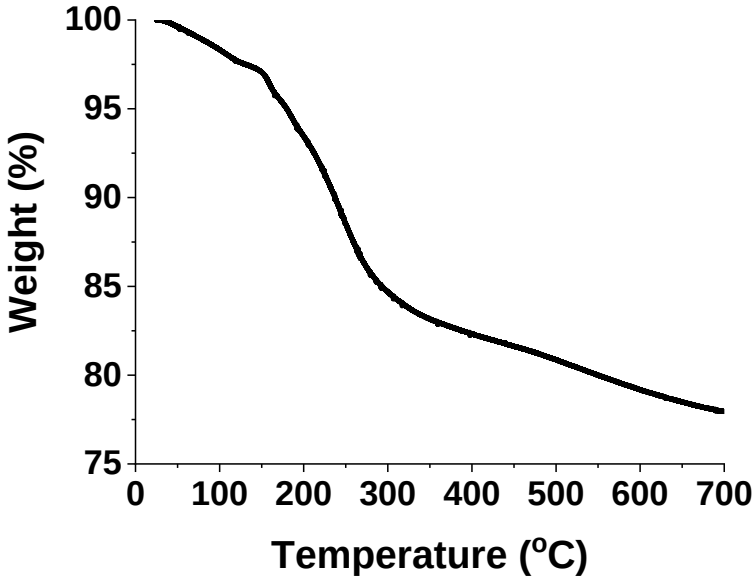

Figure 4.4 : TGA analysis of Fe doped ZnO.

Once the residue is heat treated at 500°C for 4 hours, XRD shows that (Figure 4.5) Fe doped ZnO is formed as seen in Figure 4.6. According to XRF results, after the heat treatment, the Cl amount is significantly reduced from 45.97% to 1.21% while the Zn amount is significantly increased from 52.21% to 95.70% and the Fe amount is increased from 0.88% to 1.90% thanks to the reaction given in Equation 4.6. Also, the XRD result of the HT-NL10 reveals the complete transformation to ZnO and Rietveld analysis verifies that the sample is completely transformed into ZnO with 10.69% amorphous content with 2.49 GoF. The theoretical ZnO lattice parameters (a = 3.24 Å, c = 5.22 Å) show slight changes upon Fe doping, with the "a" parameter increasing to 3.2504 Å and the "c" parameter decreasing to 5.2063 Å in the doped sample. These small shifts indicate that Fe incorporation into the ZnO lattice introduces strain, expanding the lattice in the "a" direction and slightly compressing it in the "c" direction. This demonstrates that even minimal Fe doping has a measurable effect on the ZnO crystal structure.

$$Zn(OH)_8Cl_2.H_2O \rightarrow 5ZnO + 2HCl + 4H_2O \quad (4.6)$$

Table 4.3 : XRF results after heat treatment.

	Temperature (°C)	Time (h)	Zn%	Cl%	Fe%
HT-1	400	2	93.56	2.36	1.81
HT-2	500	2	94.96	1.48	1.85
HT-3	500	4	95.70	1.21	1.90

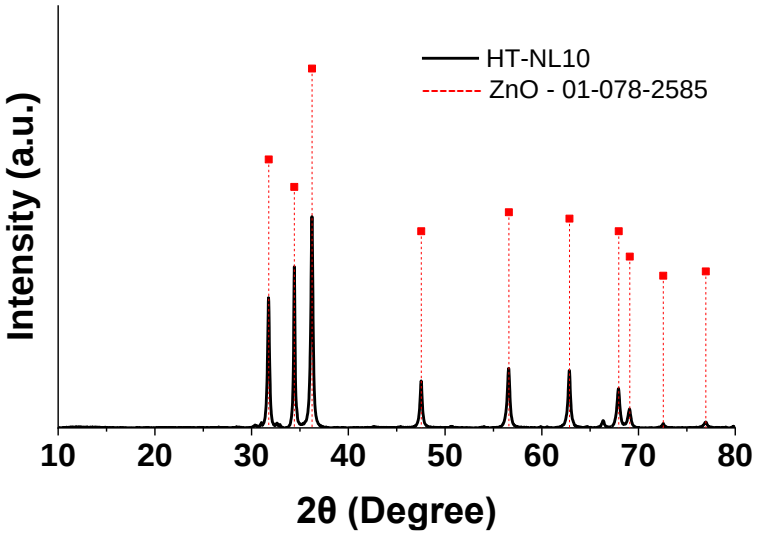

Figure 4.5 : XRD results after heat treatment at 500°C for 4 hours.

Figure 4.6 : Fe doped ZnO after heat treatment.

4.1.4 Planetary ball milling

Fe doped ZnO powder is further ball milled using zircon balls (5mm and 10mm in diameter), at 500 rpm, 60 minutes, ball to powder ratio of 20:1, vial filling ratio of 1/3 with adding 50% of particle dispersing agent amount (herein ethanol was selected). This milled Fe doped ZnO is mixed with different amounts of activated carbon: ZnO/C ratios (1/1 (C1), 2/1 (C2) and 3/1 (C3)) using planetary ball milling at 500 rpm for 1 hour with a 20:1 ball-to-powder ratio (see Figure 4.7).

SEM images seen in Figure 4.8 provide information about the morphology of the Fe doped ZnO and Fe-ZnO/C composite anodes with different ZnO/C ratios. It can be seen that all samples have uniform particle size distribution but further milling with active carbon the particle size is reduced and homogeneous particle distribution is detected.

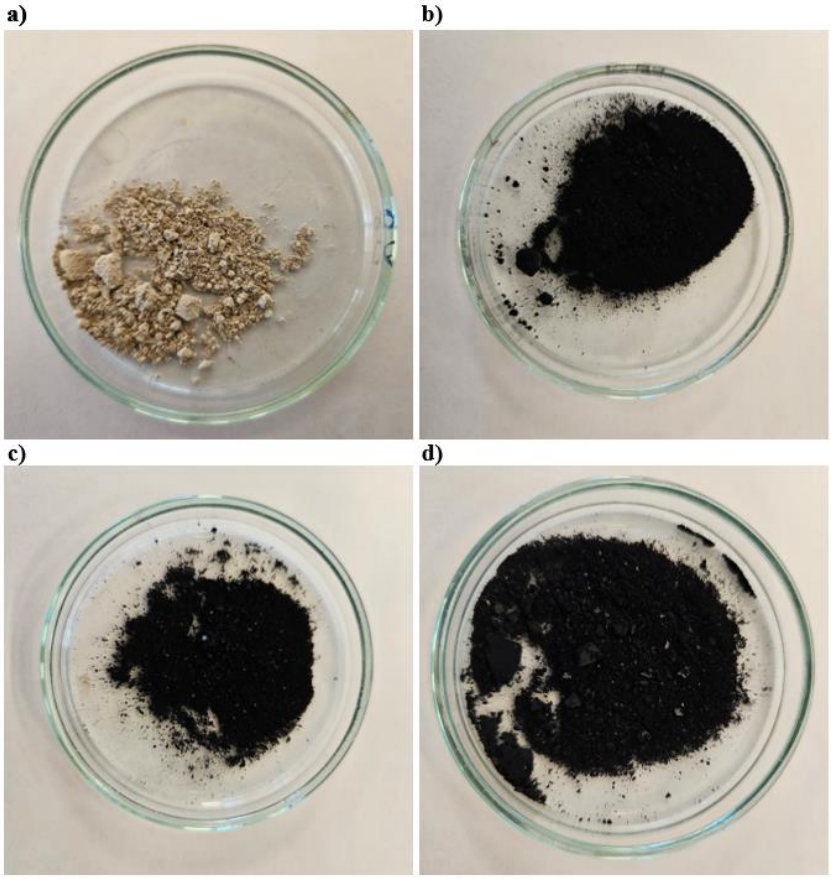

Figure 4.7 : a) Fe doped ZnO b) C1 c) C2 d) C3.

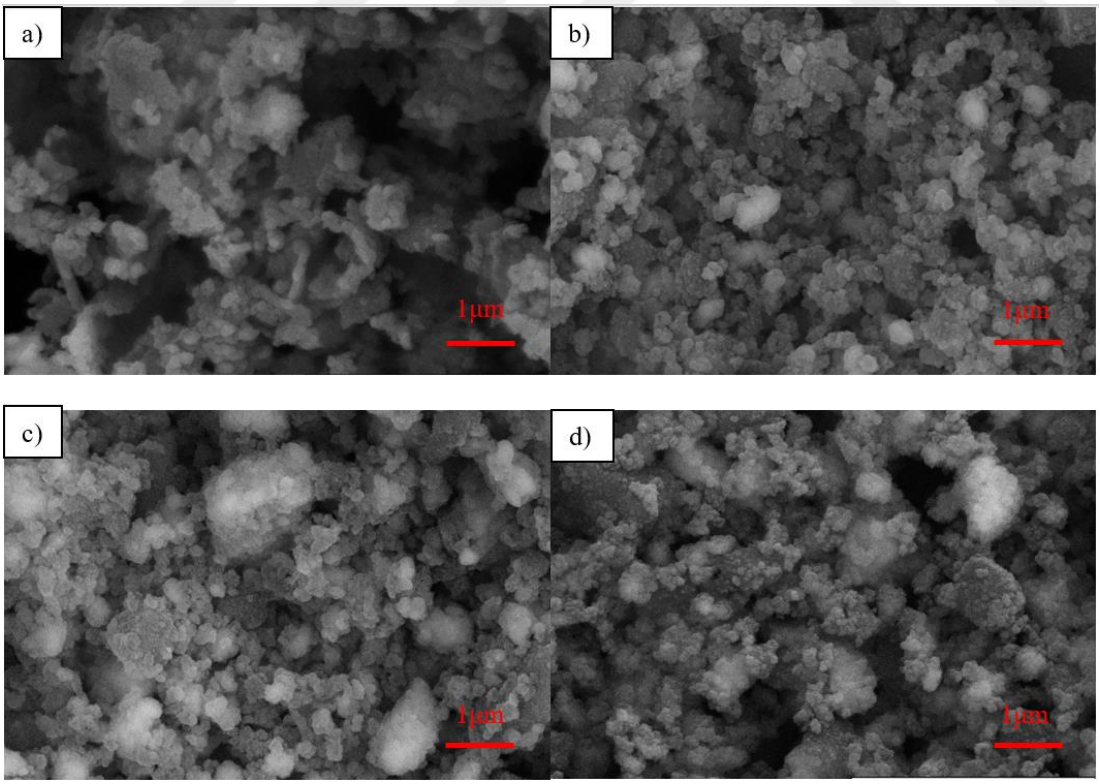

Figure 4.8 : SEM images of a) milled Fe doped ZnO b) C1 c) C2 d) C3.

XRD results of the Fe doped ZnO/C composite electrodes can be seen in Figure 4.9. It can be clearly seen that no phase transformation is seen after planetary ball milling at the defined experimental conditions and the powder remains in the form of ZnO.

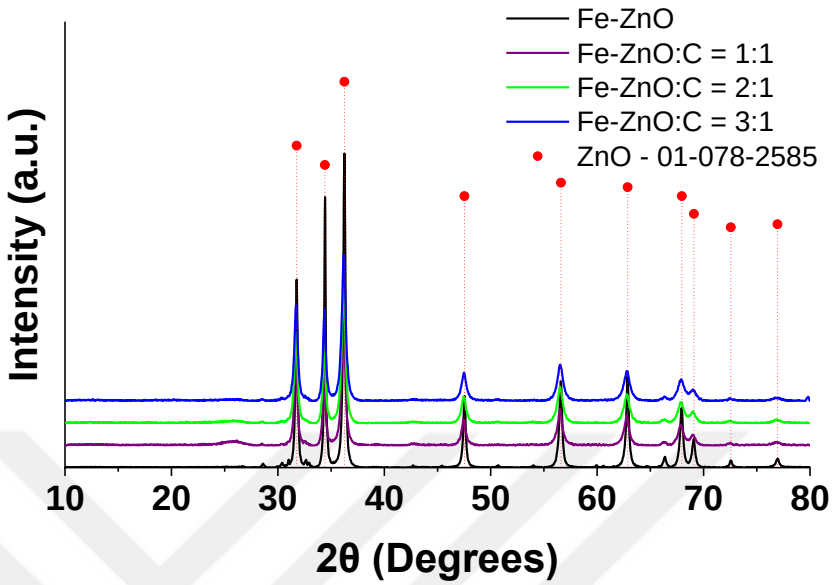

Figure 4.9 : XRD results of milled Fe doped ZnO, Fe doped ZnO/C with 1/1, 2/1 and 3/1 ZnO:C ratio.

The energy bandgap of ZnO-based materials is measured using UV-Vis spectroscopy, and the results are presented in Figure 4.10. The Tauc plot method is employed to determine the bandgap energies for Fe-doped ZnO (Fe-ZnO), and Fe-doped ZnO combined with active carbon in a 3/1 ratio (Fe-ZnO/C = 3:1 called 'C3').

$$(\alpha h\nu)^{1/r} = A(h\nu - E_g) \qquad (4.7)$$

In Equation 4.7, α represents the absorption coefficient, h is Planck's constant, ν denotes the frequency of the incident light, A is a coefficient related to the effective mass of the electron, r is 0.5 for direct band gap transitions and 2 for indirect ones, and E_g is the band gap energy [109-112]. By extrapolating the linear region, the band gap energies are calculated. Tauc plot shows that Fe doped ZnO sample has a bandgap of 2.94 eV and for C3 (Fe-doped ZnO/C with 3/1 ZnO/C) a decrease in the bandgap is calculated as 2.76 eV [113]. This significant reduction in the bandgap energy is the result of the presence of carbon [113]. Carbon could enhance the charge transfer processes and increase the electrical conductivity and this results in lowering the overall energy required for electronic transitions.

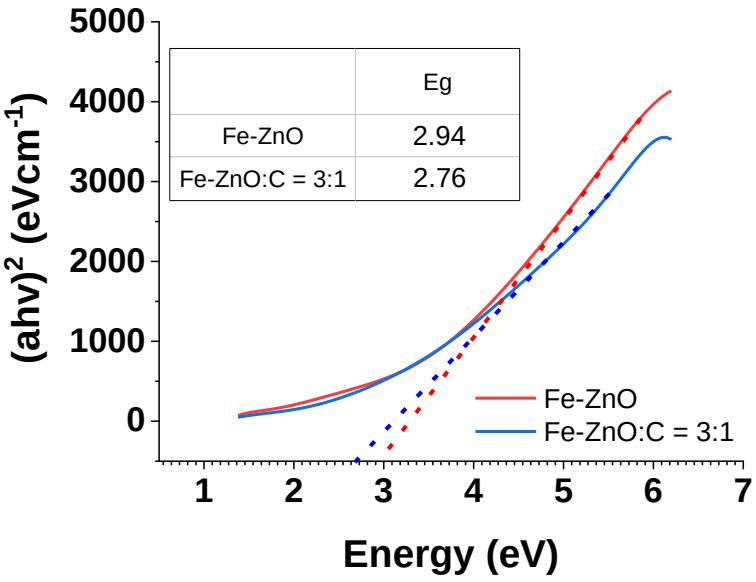

Figure 4.10 : Energy Bandgap measurements of Fe doped ZnO and Fe doped ZnO/C with 3/1 ZnO/C ratio.

4.1.5 Electrochemical characterization

The electrodes prepared for electrochemical characterization can be seen in Figure 4.11. From the pictures, it is visible that they were prepared and coated homogeneously on a copper foil with the Doctor Blade method.

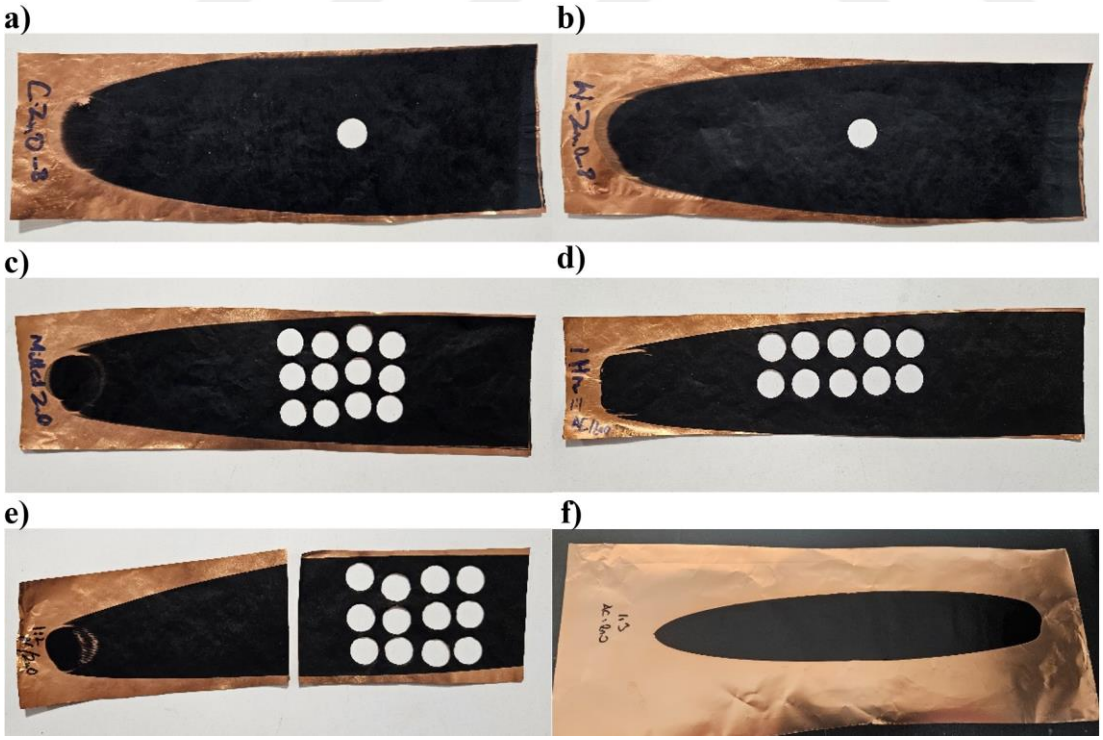

Figure 4.11 : Electrodes prepared with Doctor Blade method. a) Commercial ZnO b) Unmilled Fe doped ZnO c) milled Fe doped ZnO d) C1 e) C2 f) C3.

To discuss the electrochemical performance of the synthesized powders, it is important to evaluate the reactions that occur at the ZnO based anodes. During the charge and discharge processes, two reactions occur at the anode electrode as seen in Equations 4.8 and 4.9 [99].

Conversion:

$$ZnO + 2Li^{+} + 2e^{-} \leftrightarrow Zn + Li_2O \quad (4.8)$$

Alloying-Dealloying:

$$Zn + Li^{+} + e^{-} \leftrightarrow LiZn \quad (4.9)$$

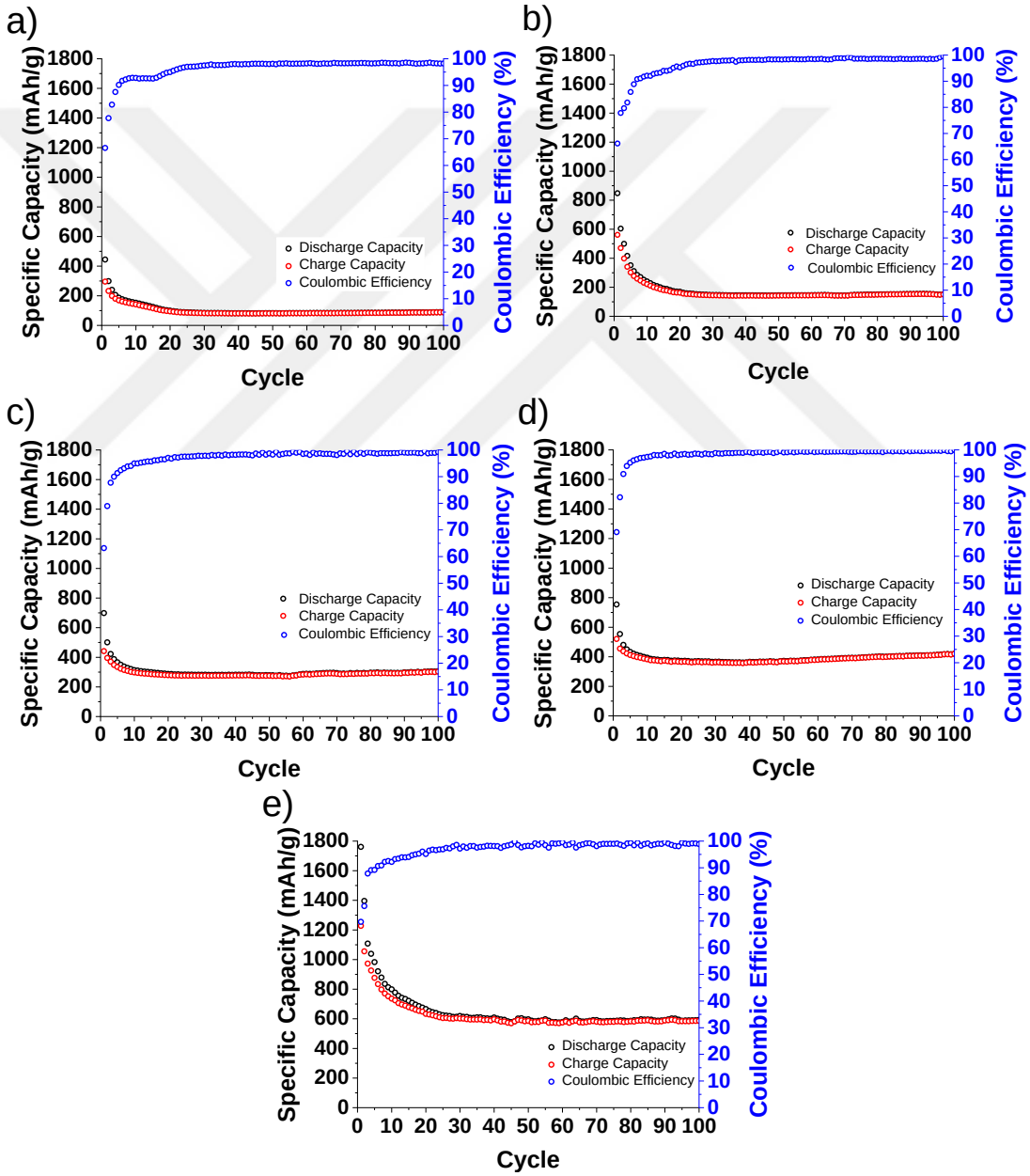

Figure 4.12 : Cycle number-Capacity curve of a) not milled Fe doped ZnO b) milled Fe doped ZnO c) C1 d) C2 e) C3.

Detailed electrochemical evaluation of the synthesized powders is accomplished by testing the electrodes galvanostatically at a current load of 50 mA/g between the voltage window of 10mV-3V. Figure 4.12 exhibits the galvanostatic test results (Capacity-Cycle) of unmilled Fe doped ZnO, milled Fe doped ZnO and three carbon composites (C1, C2, C3). Figure 4.12.a. the not milled sample which is Fe doped ZnO without any modification delivered 444.37 mAh/g specific capacity and after the 100^{th} cycle, it delivered 89.12 mAh/g specific capacity. However, the milled Fe doped ZnO shows improved electrochemical performance with 1^{st} discharge capacity of 848.35 mAh/g and after 100 cycles 151.63 mAh/g, emphasizing the importance of particle size of the anode active material on the electrochemical performance. To evaluate the effect of modifying Fe-doped ZnO anodes with carbon as a composite anode, Fe-doped ZnO/C composite anodes with different C ratios (1/1:C1, 2/1:C2, and 3/1:C3) are shown in Figure 4.12.c-e. The composites show significantly enhanced performance compared to the previous metal oxide samples thanks to their carbon content. The existence of carbon creates conductive pathways in the electrode and facilitates more efficient lithiation/delithiation processes. C1 delivered 698.53 mAh/g specific capacity at the first discharge and 306.51 mAh/g specific capacity after the 100^{th} cycle. This result shows that even though carbon addition can decrease the first cycle capacity, it provides better retention since the retention of milled Fe doped ZnO is 21.71% and the retention of C1 is 43.88%. Also, it can be seen that C2 and C3 performed better than commonly used graphite anodes (theoretical capacity of 372 mAh/g) since C2 delivered 420.49 mAh/g after 100^{th} cycle and C3 delivered 592.68 mAh/g after 100^{th} cycle. Among these composites, C3 (ZnO/C: 3/1) achieves the highest specific capacity, reaching up to 1760.72 mAh/g at the first cycle, and maintains stable voltage profiles after 25 cycles, highlighting its superior cyclic stability and capacity retention (as seen in Figure 4.12.e). The findings demonstrate that the presence of carbon strengthens the structure mechanically, increases electrical conductivity and facilitates more effective lithiation/delithiation processes that enhance capacity retention. However, scrutiny demonstrates that the Fe-ZnO/C ratio is also very important since the theoretical capacity of carbon is much lower than ZnO [114].

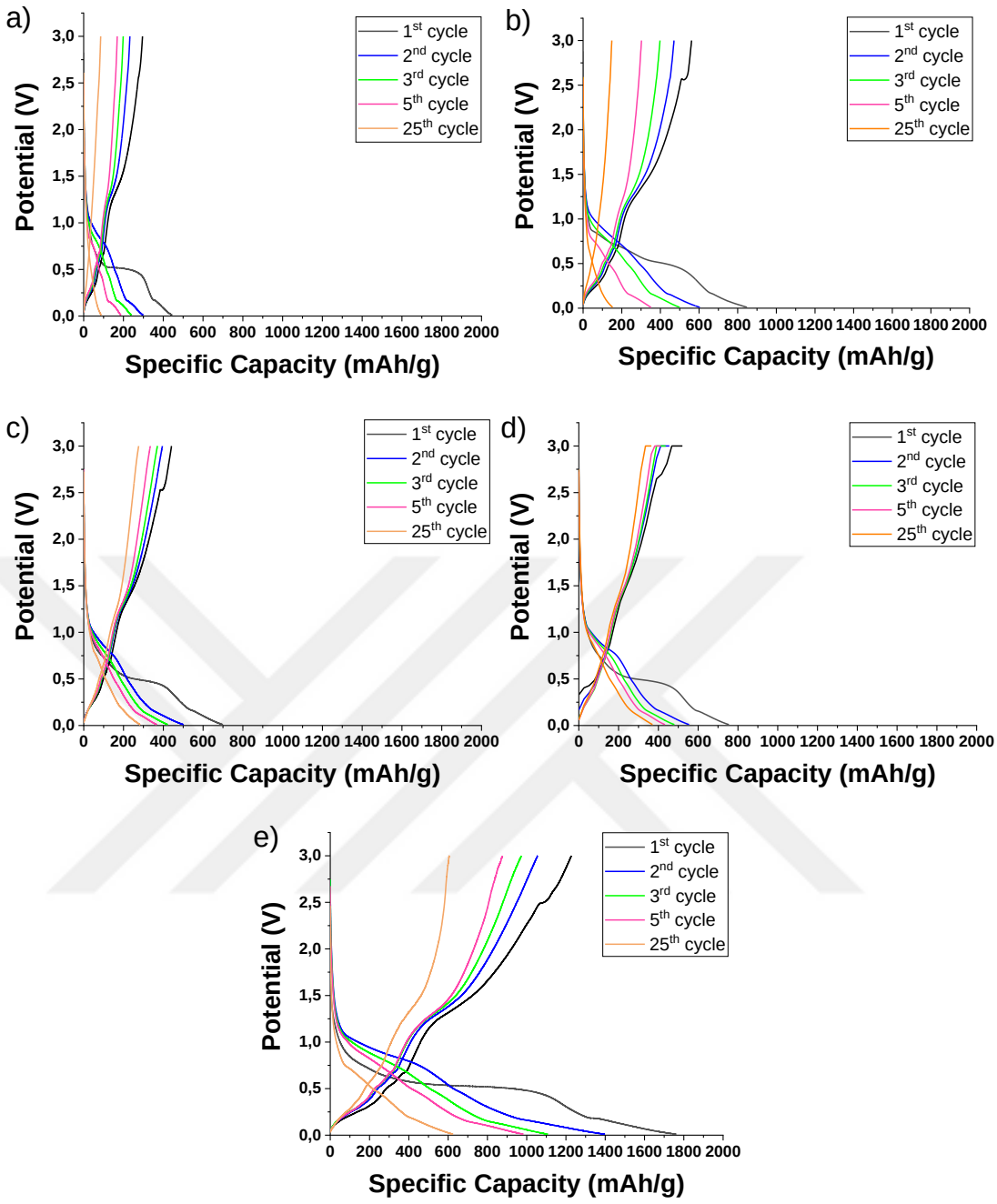

Figure 4.13 : a) Voltage-Capacity curve of a) not milled Fe doped ZnO b) milled Fe doped ZnO c) C1 d) C2 e) C3.

Figure 4.13 highlights the voltage-capacity behavior of the electrodes. ZnO based anodes undergo two types of reactions during the charge and discharge processes as seen in Equations 4.8 and 4.9.

During 1st discharge, all samples exhibited a slight plateau at 0.9V corresponding to the formation of Li_2O and Zn (Equation 4.8) then a distinct lithiation plateau around 0.5V ascribed to the formation of irreversible solid electrolyte interface (SEI) as it did not appear in the subsequent cycle [115]. Consequently, on the charge curve, a few

plateaus appear at around 0.2-0.7V, which are related to the multistep dealloying reaction of LiZn reverting LiZn to Zn, followed by the prominent plateau at 1.3V associated with ZnO formation which is known as the conversion reaction [115]. The following cycles show significant capacity fading and changes in the voltage profile, indicating limited cyclic stability and possible side reactions. The unmilled Fe-doped ZnO anode shows an initial lithiation plateau similar to the pure ZnO, but the capacity performance is slightly improved in subsequent cycles. This shows that Fe being electrochemically inactive helps to create defects in ZnO and decreases the band gap energy of the material, promoting its electrochemical behavior. An additional plateau occurring in the 1st charge curve at 2.5V could be related to electrolyte decomposition [116]. Then, in the subsequent cycles consistent capacity retention and stable voltage profiles are noted, indicating good cyclic stability [117]. The distinct voltage plateaus and capacity retention observed in the Fe-ZnO/C composites suggest a combination of reversible alloying/dealloying of Zn and the buffering effect of carbon, which mitigates volume expansion and enhances electrical conductivity. These findings indicate the potential of Fe-ZnO/C composites, especially with higher ZnO content, as promising anode materials for high-performance lithium-ion batteries [118].

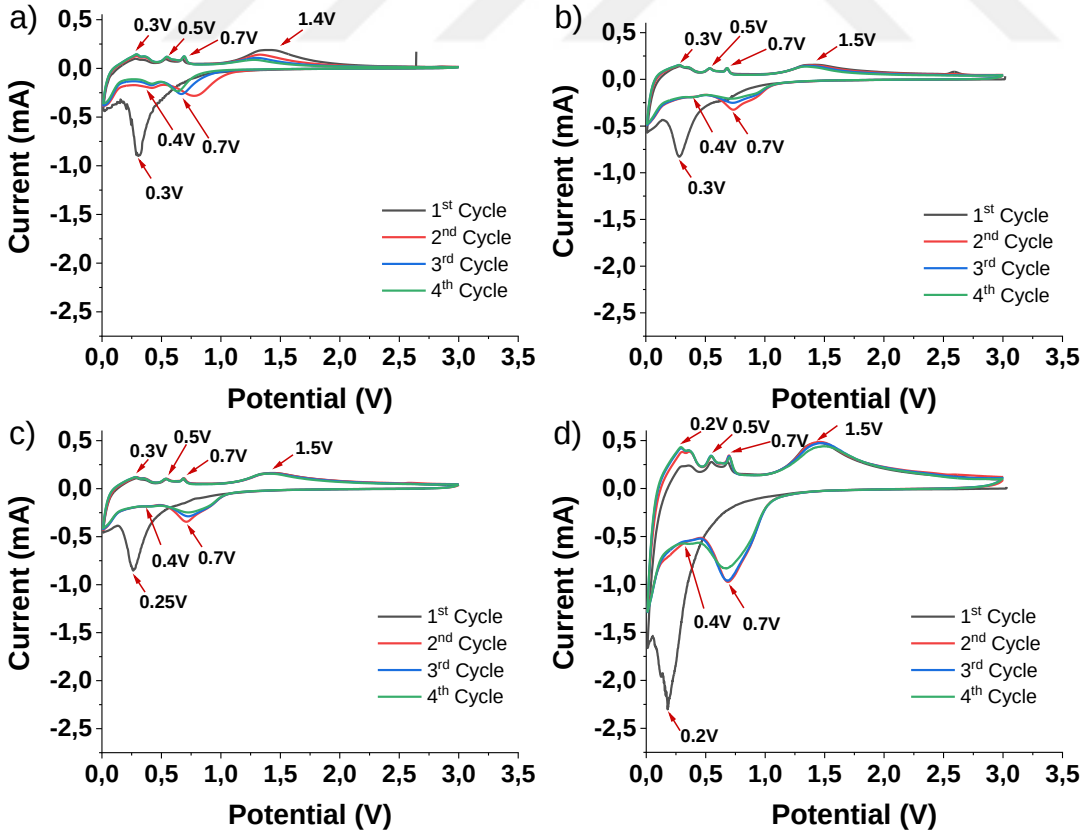

Figure 4.14 : Cyclic Voltammogram of a) milled Fe doped ZnO b) C1 c) C2 d) C3.

To get a deeper insight into the ongoing surface reaction of all electrodes, cyclic voltammetry (CV) is applied and cyclic voltammograms are exhibited in Figure 4.14. All samples exhibit similar characteristic peak shapes and positions since they consist of the same phase (ZnO) as discussed earlier. In the first cycle of Fe-ZnO, the cathodic peak appeared around 0.3V and is associated with the alloying reaction forming LiZn and the conversion reaction both [119]. This process includes the formation of a solid electrolyte interface (SEI) layer. The intense peak at 0.3V in the first cycle diminishes in subsequent cycles, indicating the formation of a stable SEI layer [116]. In the following cycles, this peak divides into two peaks: the peak at 0.4 V corresponds to the alloying reaction whereas the peak at 0.7 V, as explained in previous studies, is due to structural change that occurred in 1st cycle which results in a reduction in overpotential of the conversion reaction [99]. After the 3rd cycle the cathodic peak at 0.8V disappears and curves are overlapped, which shows the stabilization of the electrode/electrolyte interface. Then, when the CV curves of composites are studied a cathodic peak shifting to 0.2V is noted as related to the C reaction with Li [120]. At the anodic side, three small peaks are observed between 0.2V and 0.7V which indicates the multi-step dealloying process of LiZn, reverting LiZn back to Zn as in Equation 4.9 [121]. Again, at the anodic side, a major peak appeared at ~1.4V at milled Fe doped ZnO and ~1.5V at the sample with the 3/1 ZnO/C ratio. This peak shows the reversible oxidation reaction of Zn to form ZnO as seen in Equation 4.8 [117] and the shift of this peak with increasing ZnO content suggests that higher ZnO amounts lead to slightly higher polarization, likely due to reduced electron conductivity from the lower carbon content [116, 117].

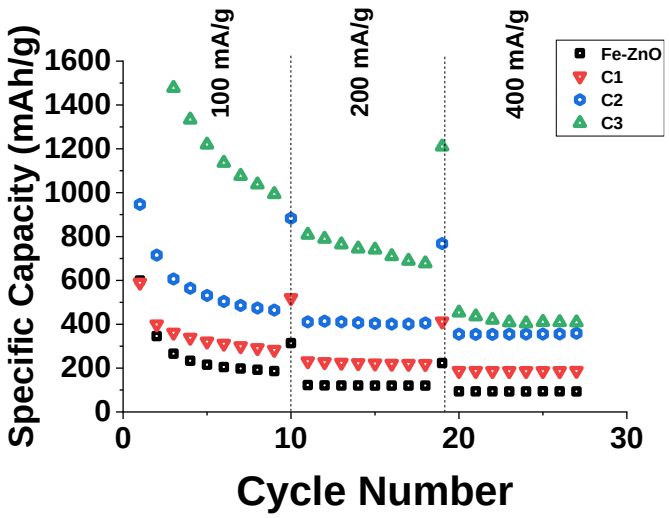

Figure 4.15 : Rate test of milled Fe doped ZnO, sample C1, C2 and C3.

To have an understanding of how these electrodes perform under different current loads, a rate test is conducted as seen in Figure 4.15. Milled Fe-doped ZnO shows low specific capacity compared to the composites, indicating that the addition of carbon improves the electrochemical performance of the Fe doped ZnO anode. C1 has a stable yet lower capacity compared to C2 and C3. C2 and C3, with higher ZnO content, show increased specific capacities. However, as the current rate increases, especially during high current loads such as 400 mA/g, an obvious capacity drop is noticed, but C3 delivered around 400 mAh/g at 400 mA/g load which is believed to be promising.

4.2 Design of $Zn_5(CO_3)_2(OH)_6$ Anodes from Hot Dip Galvanizing Dross

4.2.1 Characterization of dross

Figure 4.16 and Table 4.4 show the composition and phases of the hot dip galvanizing dross. It can be seen in XRD results that the composition consists of the ZnO phase. XRF results show us that the dross includes 0.48% Fe and 0.78% Cl. Rietveld analysis, with 4.01 GoF, showed that hot dip galvanizing dross consists of 19.09% ZnO, 11.86% Zn with 69.05% amorphous content.

Table 4.4 : XRF elemental analysis results of hot dip galvanizing dross.

(%wt.)	Zn	Cl	Fe	Al	Mg	Si	Pb	Others
Dross	97.87	0.78	0.48	0.29	0.26	0.19	0.11	0.02

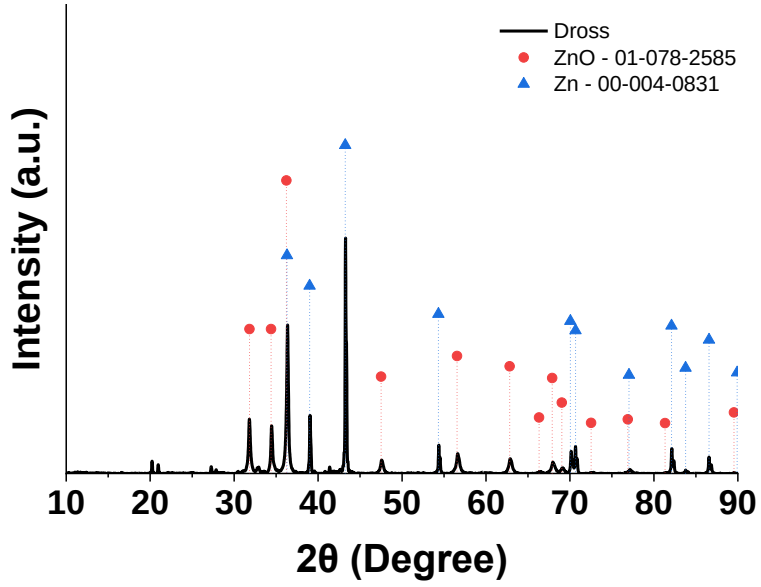

Figure 4.16 : XRD results of hot dip galvanizing dross.

After the crushing and sieving, dross that will be prepared for acid leaching that has a particle size smaller than 100 μm can be seen in Figure 4.17.

Figure 4.17 : Hot dip galvanizing dross after sieving with a 100 μm.

4.2.2 Optimization of acid leaching and chemical precipitation parameters

In the case of using 0.1M H_2SO_4, the reaction is slower and this benefits the formation of hydrozincite ($Zn_5(CO_3)_2(OH)_6$). With the parameters of 50°C, 750 rpm and 1 hour, 100% leaching efficiency is reached. After all of the hot dip galvanizing dross is leached, chemical precipitation with 0.5M ammonium carbonate $(NH_4)_2CO_3$ is conducted.

By studying the effect of parameters (temperature, mixing duration, and aging duration), it is determined that an increase in each factor positively affects the leaching efficiency. However, the effect of mixing duration is less effective than that of the other parameters. The highest efficiency is achieved with sample CP7 (77.21%) and ICP results confirm this by indicating that 21.52% of the zinc remains in the solution after chemical precipitation, where the mixing temperature is 80°C, mixing duration is 4 hours and aging duration is 24 hours as seen in Table 4.5.

After the filtration and drying, $Zn_5(CO_3)_2(OH)_6$ obtained by this process can be seen in Figure 4.18 and XRF results are seen in Table 4.6 showing that the composition mostly contains zinc (Zn) including ~1.5%wt. iron (Fe).

Table 4.5 : Optimization of chemical precipitation parameters.

Sample Code	Temperature (°C)	Mixing Duration (h)	Rotational Speed (rpm)	Waiting Duration (h)	Efficiency (%)
CP1	25	1	750	-	33.93
CP2	50	1	750	-	52.63
CP3	25	1	750	24	50.21
CP4	50	1	750	24	65.64
CP5	50	4	750	24	68.90
CP6	80	1	750	24	74.86
CP7	80	4	750	24	77.21

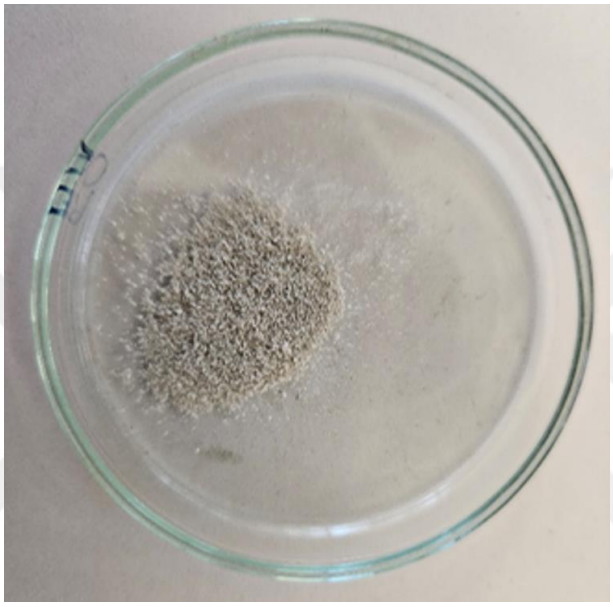

Figure 4.18 : Hydrozincite ($Zn_5(CO_3)_2(OH)_6$) obtained after chemical precipitation.

Table 4.6 : XRF result of the produced hydrozincite.

(%wt.)	**Zn**	**Fe**	**Al**	**S**	**Pb**	**Ni**	**Si**	**Others**
Hydrozincite	97.80	1.48	0.21	0.18	0.14	0.07	0.06	0.06

4.2.3 Planetary ball milling

Planetary ball milling was applied to reduce the particle size. The results of planetary ball milling can be seen in Table 4.9.

SEM images of unmilled and 1-hour milled hydrozincite can be seen in Figure 4.19. Images show that the milling resulted in much smaller and evenly distributed particle size. This will further benefit the battery formation as the smaller particles tend to react faster.

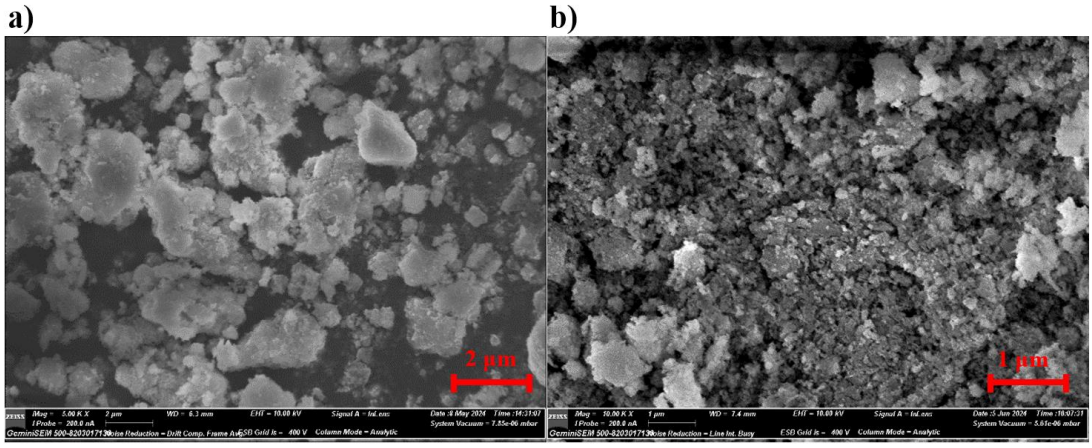

Figure 4.19 : SEM images of a) unmilled b) 1h milled hydrozincite.

XRD results of these powders can be seen in Figure 4.20. It can be seen that no phase transformation happened during planetary ball milling and the powder remains in the form of hydrozincite. Rietveld analysis, with 2.94 GoF, showed that obtained hydrozincite consists of 60.9% $Zn_5(CO_3)_2(OH)_6$, 39.1% amorphous content.

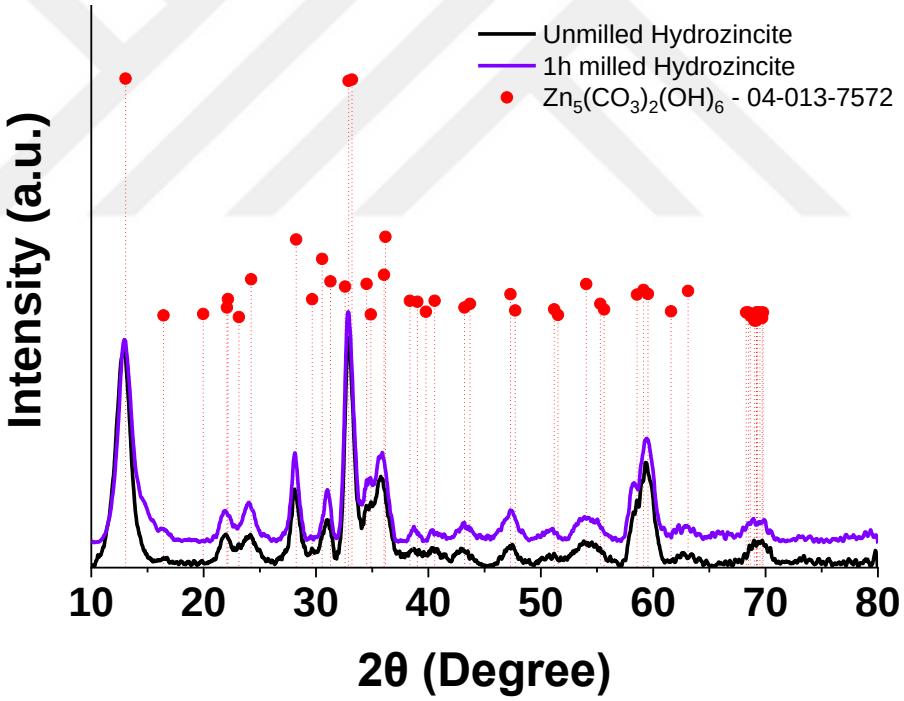

Figure 4.20 : XRD results of unmilled and 1h milled hydrozincite.

4.2.4 Electrochemical characterization

The electrodes prepared for electrochemical characterization can be seen in Figure 4.21. As can be seen, they were prepared and coated homogeneously on a copper foil with the Doctor Blade method.

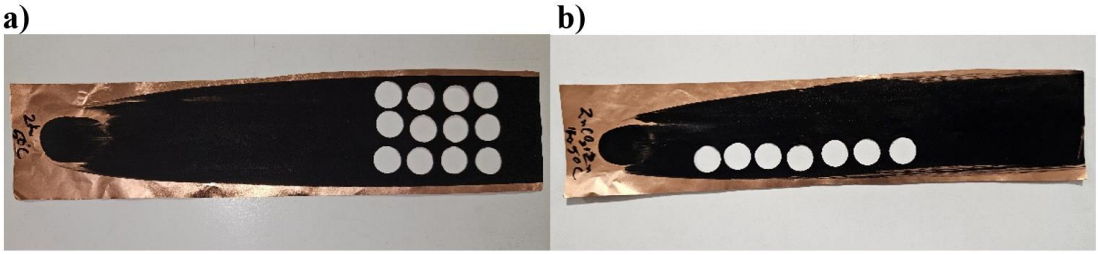

Figure 4.21 : Electrodes prepared with Doctor Blade method. a) unmilled hydrozincite b) 1h milled.

Cylcle-Capacity curve can be seen in Figure 4.22. Milled hydrozincite shows the best performance with 222.1 mAh/g after 100 cycles.

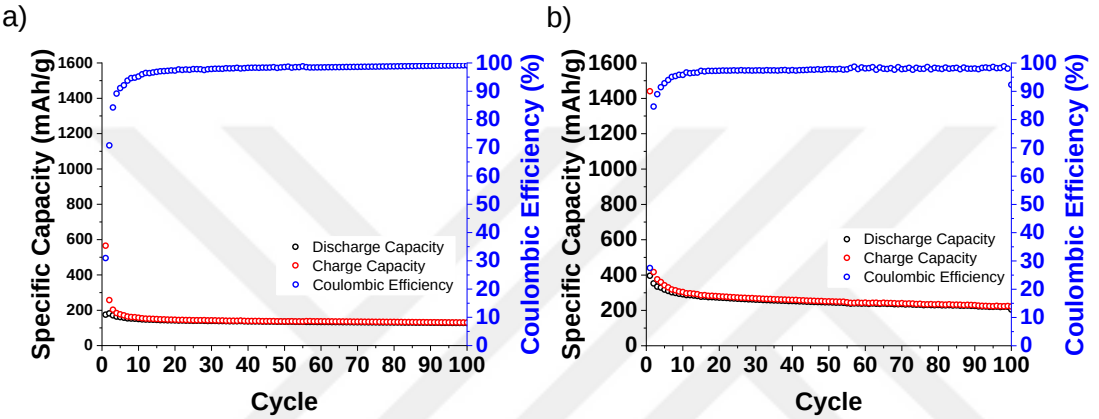

Figure 4.22 : Cycle-Capacity curve of a) unmilled b) 1h milled hydrozincite.

The voltage-capacity curve of $Zn_5(CO_3)_2(OH)_6$ can be seen in Figure 4.23. During the initial discharge cycle, the voltage profile shows a distinct plateau around 0.5-1.0 V, which corresponds to the initial lithiation process. In this phase, lithium ions intercalate into the $Zn_5(CO_3)_2(OH)_6$ structure, leading to the formation of Li_2O, LiZn, and other lithium compounds such as Li_2CO_3 and LiOH. At the milled sample, the specific capacity at the initial cycle reaches approximately 1464 mAh/g, which is significantly higher than conventional anode materials.

In the following cycles, the voltage plateaus become more stable, and the specific capacity stabilizes around 250 mAh/g. The consistent voltage profiles and specific capacities over these cycles indicate good cyclic stability and reversible lithiation/delithiation processes. This stabilization suggests that the initial structural changes during the first cycle set the stage for more stable electrochemical performance in the following cycles.

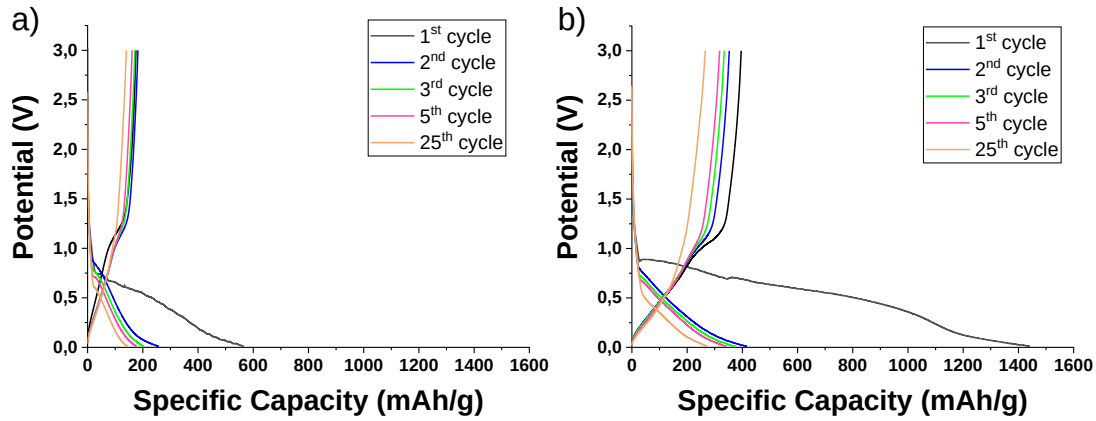

Figure 4.23 : Voltage-Capacity curve of a) unmilled hydrozincite b) 1h milled.

Cyclic voltammogram test results can be seen in Figure 4.24. The potential regions near 0.2–0.75 V may be relevant to the generation of Li_2CO_3, LiOH and Zn, accompanied by the formation of a solid electrolyte interface (SEI) [106]. The peaks in the first cycle, particularly around 0.7V and 1.1V, correspond to the reduction and oxidation of Zn-based compounds. As the number of cycles increases, the curves stabilize, especially for the milled samples, indicating better reversibility and electrochemical performance due to the structural refinement achieved by milling [21].

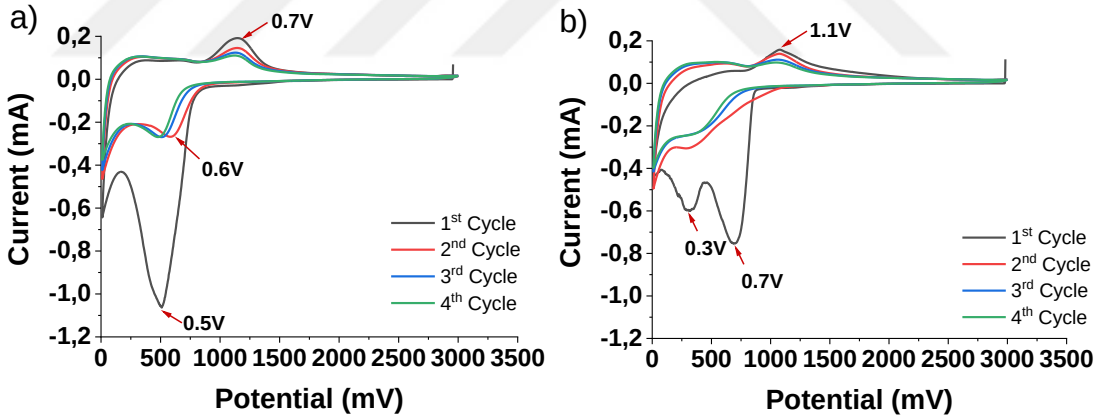

Figure 4.24 : Cyclic Voltammogram of a) unmilled hydrozincite b) 1h milled.

5. CONCLUSION

This study serves as an example that with the right material selection and process design, it is possible to produce low-carbon footprint sustainable electrode active materials from industrial waste. This thesis consists of two distinct approaches: producing a Fe-doped ZnO/C composite anode using the hot dip galvanizing waste flue dust and producing a $Zn_5(CO_3)_2(OH)_6$ anode using the hot dip galvanizing waste dross. The results have demonstrated that the two wastes generated in large quantities from the widespread hot dip galvanizing process can be transformed into a material that may be used in energy applications. This fact represents a significant advancement in the global effort to achieve carbon neutrality through environmentally sustainable methods.

In the first part of the thesis, it has been demonstrated that Fe doped ZnO can be obtained from the flue dust using a neutral leaching process. 11 experiments were conducted at different parameters (temperature, rotational speed, time and solid to liquid ratio) where the optimal conditions are found as 80°C, 750 rpm, 1 hour and 1:100 solid to liquid ratio. The results show that the most effective parameter in leaching is temperature because higher temperatures accelerate the reaction kinetics and enhance the solubility of zinc complexes and the least effective parameter is the mixing duration, as extended time does not significantly impact the concentration of Zn in the residue once the reaction has reached an optimal level. After the leaching, a 4-hour heat treatment at 500°C is conducted. XRF results show that upon the heat treatment, the concentration of Zn is significantly increased whereas the concentration of Cl is decreased: 95.7%wt. Zn, 1.2%wt. Cl and 1.9%wt. Fe. Also, XRD results show that the leach residue after neutral leaching consists of two phases which are zinc oxide (ZnO) and simonkolleite ($Zn_5(OH)_8Cl_2 \cdot H_2O$) and after the heat treatment complete ZnO structure is obtained. SEM images show that all samples have uniform particle size distribution and planetary ball milling promotes smaller sized particles formation and their homogeneous distribution. Knowing that pure ZnO has low conductivity and performs high volume expansion upon lithiation when it is used as an anode active

material, in this work Fe doped ZnO is recovered from the waste to get a powder with lower band gap energy with 2.94 eV. And Fe doped ZnO/C composite is fabricated within this concept to create conductive pathways in the electrode which reduces the polarization and improves the cycle performance of the anode active material due to the addition of carbon in the composite. The composite (Fe doped ZnO/C: 3/1) obtained from the recycling of the flue dust is galvanostatically tested against Li between 10mV-3V (vs Li/Li^+), under a current load of 50 mA/g in CR2032 coin cells, and it was observed to have a performance of 592.68 mAh/g after 100 cycles.

In the second part of the thesis, a different chemistry is studied as an anode active material. A novel flowchart is designed for the utilization of dross waste in the synthesis of hydrozincite. First, the dross is leached out using 0.1M H_2SO_4 at a pH of 3.2. With a 1:10 solid to liquid ratio, at 50°C with 750 rpm in 1 hour, 100% leaching efficiency is reached. Temperature is found to be the most effective parameter for sulfuric acid leaching, due to its impact on solubility and reaction kinetics. Next, chemical precipitation is realized by adding 135 ml of 0.5M $(NH_4)_2CO_3$ at a pH of 6.2. To optimize the chemical precipitation parameters (temperature, mixing duration, and waiting duration) 7 experiments were conducted. The highest efficiency is achieved when the mixing temperature is 80°C, the mixing duration is 4 hours, and the waiting duration is 24 hours, with an efficiency of 77.21%. Again, the temperature is the most effective parameter because of its impact on solubility and reaction kinetics whereas the mixing duration does not significantly affect efficiency. XRF results show that the produced powder contains 97.8%wt. Zn and 1.5%wt. Fe. Also, XRD results show that the hydrozincite ($Zn_5(CO_3)_2(OH)_6$) is successfully obtained. Produced hydrozincite is further ball milled and SEM images show that milling results in much smaller and evenly distributed particle size. The obtained structure contains carbonate and hydroxide groups. The potentiostatic and the galvanostatic tests reveal that during the lithiation reaction, the carbonate and hydroxide groups bond with lithium and form Li_2CO_3 and LiOH. These phases reinforce the SEI layer, while Zn forms an alloying reaction with Li, allowing the battery to operate long cycles and at high capacity. The hydrozincite ($Zn_5(CO_3)_2(OH)_6$) structure obtained from the recycling of dross is galvanostatically tested against Li between 10mV-3V (vs Li/Li^+), under a current load of 50 mA/g in CR2032 coin cells, and it delivers 222.1 mAh/g after 100 cycles.

REFERENCES

[1] **United Nations Framework Convention on Climate Change.** (n.d.). The Paris Agreement. UNFCCC. https://unfccc.int/process-and-meetings/the-paris-agreement

[2] **Li, M., Lu, J., Chen, Z., & Amine, K.** (2018). 30 years of lithium-ion batteries. *Advanced Materials*, 30(33), 1800561. doi: 10.1002/adma.201800561.

[3] **Liu, K., Liu, Y., Lin, D., Pei, A., & Cui, Y.** (2018). Materials for lithium-ion battery safety. Science advances, 4(6), eaas9820. doi: 10.1126/sciadv.aas9820

[4] **Tokura, Y., & Nagaosa, N.** (2000). Orbital physics in transition-metal oxides. *Science*, 288(5465), 462-468. doi: 10.1126/science.288.5465.462.

[5] **Ruiz, O., Clemente, C., Alonso, M., & Alguacil, F. J.** (2007). Recycling of an electric arc furnace flue dust to obtain high grade ZnO. *Journal of hazardous materials*, 141(1), 33-36. doi: 10.1016/j.jhazmat.2006.06.079

[6] **Wang, L., Zhang, G., Liu, Q., & Duan, H.** (2018). Recent progress in Zn-based anodes for advanced lithium ion batteries. *Materials Chemistry Frontiers*, 2(8), 1414-1435. doi: 10.1039/c8qm00125a.

[7] **Rao, C. N. R.** (1989). Transition metal oxides. Annual Review of Physical Chemistry, 40(1), 291-326.

[8] **Van Leeuwen, M.** (2019). Recent developments in the global zinc and HDG markets. *In Proceedings of the 25th Hot Dip Galvanizing Conference, ˇCeské Budejovice, Czech Republic* (pp. 2-4).

[9] **Kuklik, V., & Kudlacek, J.** (2016). Hot-dip galvanizing of steel structures. Butterworth-Heinemann. doi: 10.1016/C2014-0-03512-5.

[10] **Pirošková, J., Klimko, J., Trpčevská, J., Laubertová, M., Plešingerová, B., Liptai, P., ... & Oráč, D.** (2022). Characterization of Galvanizing Flue Dust and Recycling Possibilities. *Metals*, 12(5), 744. doi: 10.3390/met12050744.

[11] **Liu, Q., Cao, Y., Chen, S., Xu, X., Yao, M., Fang, J., ... & Liu, G.** (2024). Hot-Dip Galvanizing Process and the Influence of Metallic Elements on Composite Coatings. *Journal of Composites Science*, 8(5), 160. doi: 10.3390/jcs8050160.

[12] **Reiss, G., Eßl, W., Trasca, R. A., Mugrauer, C., Stefan-Kharicha, M., Kharicha, A., ... & Goodwin, F.** (2024). Development of a Dross Build-Up Growth Process Model for Hot-Dip Galvanizing Considering Surface Reaction Kinetics. *Metallurgical and Materials Transactions B*, 55(1), 53-63. doi: 10.1007/s11663-023-02921-2.

[13] **Langill, T. J.** (2003). Batch Process Hot Dip Galvanizing. doi: 10.31399/asm.hb.v13a.a0003689

[14] **American Galvanizers Association.** (2023). *Hot-dip galvanized steel Education & Resources*. https://galvanizeit.org/

[15] **Topic: Zinc industry worldwide.** (2024). *Statista.* https://www.statista.com/topics/2306/zinc/#topicOverview

[16] **Mondal, A., Halder, A. K., Nayak, S., Kumar, R. R., Chakraborty, A., Gudimetla, S. K., ... & Dubois, M.** (2024). Root cause analysis of indentation mark defect on Zn coated steel sheet in continuous galvanizing line. *Engineering Failure Analysis*, 157, 107883. doi: 10.1016/j.engfailanal.2023.107883.

[17] **Šmak, M., Kubíček, J., Kala, J., Podaný, K., & Vaněrek, J.** (2021). The influence of hot-dip galvanizing on the mechanical properties of high-strength steels. *Materials*, 14(18), 5219. doi: 10.3390/MA14185219.

[18] **Shawki, S., & Hamid, Z. A.** (2003). Effect of aluminium content on the coating structure and dross formation in the hot-dip galvanizing process. *Surface and Interface Analysis: An International Journal devoted to the development and application of techniques for the analysis of surfaces, interfaces and thin films*, 35(12), 943-947. doi: 10.1002/SIA.1608.

[19] **Bicao, P., Jianhua, W., Xuping, S., Zhi, L., & Fucheng, Y.** (2008). Effects of zinc bath temperature on the coatings of hot-dip galvanizing. *Surface and Coatings Technology*, 202(9), 1785-1788. doi: 10.1016/J.SURFCOAT.2007.07.044.

[20] **Bellini, C., Di Cocco, V., Iacoviello, F., & Mocanu, L. P.** (2022). Bath chemical composition influence on intermetallic phases damage in hot dip galvanizing. *Procedia Structural Integrity*, 39, 574-581. doi: 10.1016/j.prostr.2022.03.131.

[21] **Hanna, F., & Nassif, N.** (1984). Factors affecting the quality of hot-dip-galvanized steel sheets. *Surface technology*, 21(1), 27-37. doi: 10.1016/0376-4583(84)90145-6.

[22] **Inagaki, J. I., Sakurai, M., & Watanabe, T.** (1995). Alloying reactions in hot dip galvanizing and galvannealing processes. *ISIJ international*, 35(11), 1388-1393. doi: 10.2355/isijinternational.35.1388.

[23] **Di Cocco, V., Iacoviello, F., D'Agostino, L., & Natali, S.** (2017). Damage micromechanisms in a hot dip galvanized steel. *Procedia Structural Integrity*, 3, 231-236. doi: 10.1016/j.prostr.2017.04.054.

[24] **Elsaadawy, E. A., Hanumanth, G. S., Balthazaar, A. K. S., McDermid, J. R., Hrymak, A. N., & Forbes, J. F.** (2007). Coating weight model for the continuous hot-dip galvanizing process. *Metallurgical and Materials Transactions* B, 38, 413-424. doi: 10.1007/S11663-007-9037-2/figures/16.

[25] **Kekec, B., Bilim, N., & Ghiloufi, D.** (2018). A Review on the Evolution of the Turkey Mining Sector. Academic Perspective Procedia, 1(1), 1146-1156. doi: 10.33793/acperpro.01.01.184

[26] **Sepper, S., Peetsalu, P., Kulu, P., Saarna, M., & Mikli, V.** (2016). The role of silicon in the hot dip galvanizing process. *Proceedings of the Estonian Academy of Sciences*, 65(2). doi: 10.3176/proc.2016.2.11.

[27] **Kania, H., & Saternus, M.** (2023). Evaluation and current state of primary and secondary zinc production—a review. *Applied Sciences*, 13(3), 2003. doi: 10.3390/app13032003.

[28] **Schulz, W. D., & Thiele, M.** (2012). General hot-dip galvanizing. *Eugene Leuzeverlag KG*.

[29] **Dallin, G. W.** (2017). Galvanizing—2014 continuous hot-dip galvanizing—process and prodcuts.

[30] **Allied Market Research, https://www.alliedmarketresearch.com/.** (n.d.). Hot-Dip Galvanized Steel Market Size, Share, Competitive Landscape and Trend Analysis Report, By product type, By End Use Industry : Global Opportunity Analysis and Industry Forecast, 2023-2032. Allied Market Research. https://www.alliedmarketresearch.com/hot-dip-galvanized-steel-market-A113149

[31] **Jastrzębski, K., & Ślęczka, L.** (2023). Experimental study on the slip factor coefficient of wet and dry hot-dip galvanised surfaces. *Inżynieria i Budownictwo*, 79(9-10), 474-478. doi: 10.5604/01.3001.0053.8870.

[32] **Liu, Q., Cao, Y., Chen, S., Xu, X., Yao, M., Fang, J., ... & Liu, G.** (2024). Hot-Dip Galvanizing Process and the Influence of Metallic Elements on Composite Coatings. *Journal of Composites Science*, 8(5), 160. doi: 10.3390/JCS8050160.

[33] **Warichet, D., Kone, G., & Vervisch, A.** (2009). WO2010081905A1 - Flux and fluxing bath for hot dip galvanization, process for the hot dip galvanization of an iron or steel article

[34] **Cieplak, A., Gdoura, A., Gay, B., Portebois, L., Ramenatte, N., Proriol Serre, I., & Balloy, D.** (2023). New protective coatings against liquid zinc corrosion. *SN Applied Sciences*, 5(5), 142. doi: 10.1007/S42452-023-05319-6/figures/6.

[35]**Gogola, P., Gabalcová, Z., Suchánek, H., & Kusý, M.** (2020). Intermetallics formation during hot dip galvanizing of high carbon steel. *In IOP Conference Series: Materials Science and Engineering* (Vol. 723, No. 1, p. 012007). IOP Publishing. doi: 10.1088/1757-899X/723/1/012007.

[36] **Ploypech, S., Jearanaisilawong, P., & Boonyongmaneerat, Y.** (2013). Influence of thickness of intermetallic layers on fracture resistance of galvanized coatings. *Surface and Coatings Technology*, 223, 1-5. doi: 10.1016/j.surfcoat.2013.02.017.

[37] **Rabah, M. A., Barakat, M. A., & Mahrous, Y. S.** (1999). Recovering metal values hydrometallurgically from spent dry battery cells. *JOM*, 51(12), 41-43. doi: 10.1007/s11837-999-0171-y.

[38] **Dakhili, N., Razavizadeh, H., Salehi, M. T., & Seyedein, S. H.** (2011). Recovery of zinc from the final slag of steel's galvanizing process. *Advanced Materials Research*, 264, 592-596. doi: 10.4028/www.scientific.net/AMR.264-265.592.

[39] **Rabah, M. A., & El-Sayed, A. S.** (1995). Recovery of zinc and some of its valuable salts from secondary resources and wastes. *Hydrometallurgy*, 37(1), 23-32. doi: 10.1016/0304-386x(94)00015-u.

[40] **Long, H., Tan, X., Ni, S., Ma, A., Li, S., & Zhu, D.** (2023). Ammoniacal leaching behavior and regularity of zinc ash. *International Journal of Chemical Reactor Engineering*, 21(7), 895-906. doi: 10.1515/IJCRE-2022-0087.

[41] **Wang, S., Zhang, J., Shen, Y., & Zhang, J.** (2024). Preparation of nano zinc oxide by alkaline treatment of industrial zinc oxide dust. *Journal of Cleaner Production*, 434, 140107. doi: 10.1016/j.jclepro.2023.140107.

[42] **Leclerc, N., Meux, E., & Lecuire, J. M.** (2003). Hydrometallurgical extraction of zinc from zinc ferrites. *Hydrometallurgy*, 70(1-3), 175-183. doi: 10.1016/S0304-386X(03)00079-3

[43] **Rudnik, E.** (2020). Hydrometallurgical recovery of zinc from industrial hot dipping top ash. *Transactions of Nonferrous Metals Society of China*, 30(8), 2239-2255. doi: 10.1016/S1003-6326(20)65375-4.

[44] **Dudek, F. J., Daniels, E. J., & Morgan, W. A.** (1993). *Recycling galvanized steel: Operating experience and benefits* (No. ANL/ES/CP-80360; CONF-9310158-1). Argonne National Lab., IL (United States).

[45] **Iluțiu-Varvara, D. A., & Aciu, C.** (2022). Metallurgical wastes as resources for sustainability of the steel industry. Sustainability, 14(9), 5488. doi: 10.3390/su14095488

[46] **Montes Villasana, P.** (2019). Zinc recovery technologies from solid wastes of hot dip galvanizing.

[47] **Vlad, M., Movileanu, G., Radu, T., & Balint, L.** (2011). RECYCLING OF ZINC BY-PRODUCTS. *International Multidisciplinary Scientific GeoConference: SGEM*, 3, 875.

[48] **Gel, V. I., & Sapozhkov, S. B.** (2020). Processing of steel galvanizing waste using the method of melt immersion. *In IOP Conference Series: Materials Science and Engineering* (Vol. 939, No. 1, p. 012024). IOP Publishing. doi: 10.1088/1757-899X/939/1/012024.

[49] **Takácová, Z., Hluchánová, B., & Trpcevská, J.** (2010). Leaching of zinc from zinc ash originating from hot-dip galvanizing. *Metall*, 64(12), 600.

[50] **Baik, D. S., & Fray, D. J.** (2001). Electrodeposition of zinc from high acid zinc chloride solutions. *Journal of applied electrochemistry*, 31, 1141-1147. doi: 10.1023/A:1012290132379.

[51] **Rämä, M., Jokilaakso, A., Klemettinen, L., Salminen, J., & Taskinen, P.** (2018). Experimental investigation of pyrometallurgical treatment of zinc residue. *In Extraction 2018: Proceedings of the First Global Conference on Extractive Metallurgy* (pp. 981-992). Springer International Publishing. doi: 10.1007/978-3-319-95022-8_79.

[52] **Binnemans, K., Jones, P. T., Manjón Fernández, Á., & Masaguer Torres, V.** (2020). Hydrometallurgical processes for the recovery of metals from steel industry by-products: a critical review. *Journal of Sustainable Metallurgy*, 6, 505-540. doi: 10.1007/S40831-020-00306-2.

[53] **Rudnik, E.** (2023). Hydrometallurgical Recovery of Zinc from By-Products and Waste Materials of Hot-Dip Galvanizing Process. *In Recycling Technologies for Secondary Zn-Pb Resources* (pp. 205-234). Cham: Springer International Publishing. doi: 10.1007/978-3-031-14685-5_6

[54] **Li, Y., Feng, H., Wang, J., She, X., Wang, G., Zuo, H., & Xue, Q.** (2022). Current status of the technology for utilizing difficult-to-treat dust and sludge produced from the steel industry. *Journal of cleaner production*, 367, 132909. doi: 10.1016/j.jclepro.2022.132909.

[55] **Chen, B., Yi, X., Zhan, W., Gao, L., He, Z., & Zhang, J.** (2023). Pyrometallurgical recovery of zinc and valuable metals from hazardous blast furnace dust via self-reduction roasting: Phase transformations and morphological evolution. *Materials Today Sustainability*, 24, 100590. doi: 10.1016/j.mtsust.2023.100590.

[56] **Habibie, M. H., Krismastuti, F. S. H., Septama, A. W., Maryani, F., & Fauzia, V.** (2024). Novel synthesis of ZnO nanostructure from galvanization waste for antibacterial application. *Materials Letters*, 356, 135603. doi: 10.1016/j.matlet.2023.135603.

[57] **Dvořák, P., & Jandova, J.** (2005). Hydrometallurgical recovery of zinc from hot dip galvanizing ash. *Hydrometallurgy*, 77(1-2), 29-33. doi: 10.1016/J.HYDROMET.2004.10.007.

[58] **Tan, R., & Khoo, H. H.** (2005). Zinc Casting and Recycling (8 pp). *The International Journal of Life Cycle Assessment*, 10, 211-218. doi: doi.org/10.1065/lca2004.08.172.

[59] **Wiaux, J. P.** (2017). Recycling of Zinc-Containing Secondary Products from the Galvanising and Steel Industries: A new case of applied industrial ecology. *In Perspectives on Industrial Ecology* (pp. 112-119). Routledge. doi: 10.4324/9781351282086-12.

[60] **Røine, K., & Brattebø, H.** (2017). Towards a methodology for assessing effectiveness of recovery systems: a process system approach. *In Perspectives on industrial ecology* (pp. 101-111). Routledge. doi: 10.4324/9781351282086-11.

[61] **Şahin, F. Ç., Derin, B., & Yücel, O.** (2000). Chloride removal from zinc ash. *Scandinavian journal of metallurgy*, 29(5), 224-230. doi: 10.1034/j.1600-0692.2000.d01-26.x.

[62] **Erkman, S.** (2017). Perspectives on industrial ecology. *In Perspectives on Industrial Ecology* (pp. 338-342). Routledge. doi: 10.4324/9781351282086.

[63] **Barakat, M. A.** (2003). The pyrometallurgical processing of galvanizing zinc ash and flue dust. JOM, 55(8), 26-29. doi: 10.1007/s11837-003-0100-4

[64] **Beguin, F., & Frackowiak, E.** (2009). *Carbons for electrochemical energy storage and conversion systems.* Crc Press. doi: 10.1201/9781420055405

[65] **Vourlias, G., Pistofidis, N., Pavlidou, E., Stergioudis, G., & Polychroniadis, E. K.** (2007). Study of the structure of hot-dip galvanizing byproducts. *Journal of optoelectronics and advanced materials*, 9(9), 2937.

[66] **Liptai, P., Nagy, Š., Dolník, B., Matvija, M., & Pirošková, J.** (2024). Optimization of technological processes in the manufacturability of varistors based on recycled ZnO product, with emphasis on environmental sustainability. *Heliyon*, 10(16). doi: 10.1016/j.heliyon.2024.e35898

[67] **Pirošková, J., Klimko, J., Ružičková, S., Laubertová, M., Marcinov, V., Múdra, E., ... & Oráč, D.** (2024). Utilization of Galvanizing Flue Dust Residue: A Sustainable Approach towards Complete Material Recycling. *Metals*, 14(3), 253. doi: 10.3390/MET14030253.

[68] **Xu, J., Dou, S., Liu, H., & Dai, L.** (2013). Cathode materials for next generation lithium ion batteries. *Nano Energy*, 2(4), 439-442. doi: 10.1016/j.nanoen.2013.05.013.

[69] **Xing, J., Bliznakov, S., Bonville, L., Oljaca, M., & Maric, R.** (2022). A review of nonaqueous electrolytes, binders, and separators for lithium-ion batteries. *Electrochemical Energy Reviews*, 5(4), 14. doi: 10.1007/S41918-022-00131-Z.

[70] **Korthauer, R.** (2018). *Lithium-ion batteries: basics and applications.* Springer. doi: 10.1007/978-3-662-53071-9/COVER.

[71] **What are Lithium-Ion batteries? | UL research Institutes.** (n.d.). https://ul.org/research/electrochemical-safety/getting-started-electrochemical-safety/what-are-lithium-ion

[72] **Barbosa, J. C., Dias, J. P., Lanceros-Méndez, S., & Costa, C. M.** (2018). Recent advances in poly (vinylidene fluoride) and its copolymers for lithium-ion battery separators. *Membranes*, 8(3), 45. doi: 10.3390/membranes8030045.

[73] **Melot, B. C., & Tarascon, J. M.** (2013). Design and preparation of materials for advanced electrochemical storage. *Accounts of chemical research*, 46(5), 1226-1238. doi: 10.1021/ar300088q

[74] **Ebin, B.** (2014). *Lityum İyon Pilleri İçin Nanoyapılı Ve Yüksek Kapasiteli Katot Malzemelerinin Aerosol Tekniği İle Üretimi* (Doctoral dissertation, Fen Bilimleri Enstitüsü).

[75] **Courtney, I. A.** (1999). The physics and chemistry of metal oxide composites as anode materials for lithium-ion batteries.

[76] **Wang, L. P., Yu, L., Wang, X., Srinivasan, M., & Xu, Z. J.** (2015). Recent developments in electrode materials for sodium-ion batteries. *Journal of Materials Chemistry A*, 3(18), 9353-9378. doi: 10.1039/C4TA06467D.

[77] **McDowell, M. T., Lee, S. W., Nix, W. D., & Cui, Y.** (2013). 25th anniversary article: understanding the lithiation of silicon and other alloying anodes for lithium-ion batteries. *Advanced materials*, 25(36), 4966-4985. doi: 10.1002/ADMA.201301795.

[78] **Liu, Z. G., Du, R., He, X. X., Wang, J. C., Qiao, Y., Li, L., & Chou, S. L.** (2021). Recent progress on intercalation-based anode materials for low-cost sodium-ion batteries. ChemSusChem, 14(18), 3724-3743. doi: 10.1002/cssc.202101186

[79] **Jow, T. R., Xu, K., Borodin, O., & Ue, M. (Eds.).** (2014). *Electrolytes for lithium and lithium-ion batteries* (Vol. 58, p. 476). New York: Springer. doi: 10.1007/978-1-4939-0302-3

[80] **Xu, K.** (2004). Nonaqueous liquid electrolytes for lithium-based rechargeable batteries. *Chemical reviews*, 104(10), 4303-4418. doi: 10.1021/CR030203G/ASSET/CR030203G.FP.PNG_V03.

[81] **Peled, E.** (1979). The electrochemical behavior of alkali and alkaline earth metals in nonaqueous battery systems—the solid electrolyte interphase model. *Journal of The Electrochemical Society*, 126(12), 2047. doi: 10.1149/1.2128859/XML.

[82] **Aurbach, D.** (2000). Review of selected electrode–solution interactions which determine the performance of Li and Li ion batteries. *Journal of Power Sources*, 89(2), 206-218. doi: 10.1016/S0378-7753(00)00431-6.

[83] **Borah, R., Hughson, F. R., Johnston, J., & Nann, T.** (2020). On battery materials and methods. *Materials Today Advances*, 6, 100046. doi: 10.1016/J.MTADV.2019.100046.

[84] **Sun, X., Zhang, X., Wang, K., An, Y., Zhang, X., Li, C., & Ma, Y.** (2022). Determination strategy of stable electrochemical operating voltage window for practical lithium-ion capacitors. *Electrochimica Acta*, 428, 140972. doi: 10.1016/J.ELECTACTA.2022.140972.

[85] **Smart, M. C., Hwang, C., Krause, F. C., Soler, J., West, W. C., Ratnakumar, B. V., & Amine, K.** (2013). Wide operating temperature range electrolytes for high voltage and high specific energy Li-ion cells. *ECS Transactions*, 50(26), 355. doi: 10.1149/05026.0355ECST/XML.

[86] **Cheng, X. B., Zhang, R., Zhao, C. Z., Wei, F., Zhang, J. G., & Zhang, Q.** (2016). A review of solid electrolyte interphases on lithium metal anode. *Advanced science*, 3(3), 1500213. doi: 10.1002/advs.201500213.

[87] **Suo, L., Oh, D., Lin, Y., Zhuo, Z., Borodin, O., Gao, T., ... & Wang, C.** (2017). How solid-electrolyte interphase forms in aqueous electrolytes. *Journal of the American Chemical Society*, 139(51), 18670-18680. doi: 10.1021/jacs.7b10688.

[88] **Verma, P., Maire, P., & Novák, P.** (2010). A review of the features and analyses of the solid electrolyte interphase in Li-ion batteries. *Electrochimica Acta*, 55(22), 6332-6341. doi: 10.1016/j.electacta.2010.05.072.

[89] **Takenaka, N., Bouibes, A., Yamada, Y., Nagaoka, M., & Yamada, A.** (2021). Frontiers in theoretical analysis of solid electrolyte interphase formation mechanism. *Advanced Materials*, 33(37), 2100574. doi: 10.1002/adma.202100574.

[90] **Heiskanen, S. K., Kim, J., & Lucht, B. L.** (2019). Generation and evolution of the solid electrolyte interphase of lithium-ion batteries. *Joule*, 3(10), 2322-2333. doi: 10.1016/j.joule.2019.08.018.

[91] **Beheshti, S. H., Javanbakht, M., Omidvar, H., Hosen, M. S., Hubin, A., Van Mierlo, J., & Berecibar, M.** (2022). Development, retainment, and assessment of the graphite-electrolyte interphase in Li-ion batteries regarding the functionality of SEI-forming additives. *Iscience*, 25(3). doi: 10.1016/j.isci.

[92] **Peled, E., & Menkin, S.** (2017). SEI: past, present and future. *Journal of The Electrochemical Society*, 164(7), A1703. doi: 10.1149/2.1441707jes.

[93] **Cabana, J., Monconduit, L., Larcher, D., & Palacin, M. R.** (2010). Beyond intercalation-based Li-ion batteries: the state of the art and challenges of electrode materials reacting through conversion reactions. *Advanced materials*, 22(35), E170-E192. doi: 10.1002/adma.201000717.

[94] **Whittingham, M. S.** (2014). Ultimate limits to intercalation reactions for lithium batteries. *Chemical reviews*, 114(23), 11414-11443. doi: 10.1021/cr5003003.

[95] **Liu, Y.** (2017). The development history of cathode and anode materials of lithium ion battery. *In 7th International Conference on Education, Management, Information and Mechanical Engineering (EMIM 2017)* (pp. 1395-1398). Atlantis Press. doi: 10.2991/emim-17.2017.279

[96] **Nazar, L. F., & Crosnier, O.** (2009). Anodes and composite anodes: an overview. *Lithium batteries: science and technology*, 112-143. https://doi.org/10.1007/978-0-387-92675-9_4

[97] **Xu, Y., Liu, Q., Zhu, Y., Liu, Y., Langrock, A., Zachariah, M. R., & Wang, C.** (2013). Uniform nano-Sn/C composite anodes for lithium ion batteries. *Nano letters*, 13(2), 470-474. doi: 10.1021/nl303823k.

[98] **Lobato, N. C. C., Villegas, E. A., & Mansur, M. B.** (2015). Management of solid wastes from steelmaking and galvanizing processes: A brief review. *Resources, Conservation and Recycling*, 102, 49-57. doi: 10.1016/j.resconrec.2015.05.025.

[99] **Bui, V. K. H., Pham, T. N., Hur, J., & Lee, Y. C.** (2021). Review of ZnO binary and ternary composite anodes for lithium-ion batteries. *Nanomaterials*, 11(8), 2001., doi: 10.3390/NANO11082001.

[100] **Yan, Y., Zhang, Y., Wu, Y., Wang, Z., Mathur, A., Yang, H., ... & Liu, N.** (2018). A lasagna-inspired nanoscale ZnO anode design for high-energy rechargeable aqueous batteries. *ACS Applied Energy Materials*, 1(11), 6345-6351. doi: 10.1021/acsaem.8b01321.

[101] **Wen, G., Tan, L., Lan, X., Zhang, H., Hu, R., Yuan, B., ... & Zhu, M.** (2021). Li2CO3 induced stable SEI formation: An efficient strategy to boost reversibility and cyclability of Li storage in SnO2 anodes. *Science China Materials*, 64(11), 2683-2696. doi: 10.1007/s40843-021-1665-1.

[102] **Aragón, M. J., Pérez-Vicente, C., & Tirado, J. L.** (2007). Submicronic particles of manganese carbonate prepared in reverse micelles: A new electrode material for lithium-ion batteries. *Electrochemistry communications*, 9(7), 1744-1748. doi: 10.1016/J.ELECOM.2007.03.031.

[103] **Zhang, R., Zhang, F., Feng, J., & Qian, Y.** (2014). Green and facile synthesis of porous ZnCO3 as a novel anode material for advanced lithium-ion batteries. *Materials Letters*, 118, 5-7. doi: 10.1016/j.matlet.2013.12.028.

[104] **Li, J., Li, M., Guo, C., & Zhang, L.** (2018). Recent progress and challenges of micro-/nanostructured transition metal carbonate anodes for lithium ion batteries. *European Journal of Inorganic Chemistry*, 2018(41), 4508-4521. doi: 10.1002/ejic.201800853.

[105] **Wang, L., Tang, W., Jing, Y., Su, L., & Zhou, Z.** (2014). Do transition metal carbonates have greater lithium storage capability than oxides? A case study of monodisperse CoCO3 and CoO microspindles. *ACS applied materials & interfaces*, 6(15), 12346-12352. doi: 10.1021/am5021233.

[106] **Han, W., Yang, K., Li, D., Zhang, Z., Ma, J., Ni, S., & Yang, X.** (2016). The fabrication and characterization of Zn5 (CO3) 2 (OH) 6 as a new anode material for lithium ion batteries. *Materials Letters*, 164, 148-151. doi: 10.1016/j.matlet.2015.10.102.

[107] **Burns, J. C., Krause, L. J., Le, D. B., Jensen, L. D., Smith, A. J., Xiong, D., & Dahn, J. R.** (2011). Introducing symmetric Li-ion cells as a tool to study cell degradation mechanisms. *Journal of The Electrochemical Society*, 158(12), A1417. doi: 10.1149/2.084112JES/XML.

[108] **Li, Y., Zou, Y., & Hou, Y.** (2011). Synthesis and characterization of simonkolleite nanodisks and their conversion into ZnO nanostructures. *Crystal Research and Technology*, 46(3), 305-308. doi: 10.1002/CRAT.201000673.

[109] **Rahman, M. M., Hussain, M. M., & Asiri, A. M.** (2017). Fabrication of 3-methoxyphenol sensor based on Fe3O4 decorated carbon nanotube nanocomposites for environmental safety: Real sample analyses. *PLoS One*, 12(9), e0177817.

[110] **Sunny, A., Prasad, N., Subbaiyan, D., Dillibabu, S., & Balasubramanian, K.** (2018). Optical, vibrational and fiber optic gas-sensing properties of hematite microparticles. *Applied Physics A*, 124, 1-8. doi: 10.1007/S00339-018-2077-4.

[111] **Ashraf, H., & Karahan, B. D.** (2024). Cryo-Assisted Nitrogen Treatment for the Fabrication of Nanoengineered, Mixed Transition Metal Oxide Anode from Inorganic Domestic Waste, for Lithium-Ion Batteries. *Journal of Sustainable Metallurgy*, 10(3), 1702-1716. doi: 10.1007/s40831-024-00891-6

[112] **Lv, J., Li, C., & Chai, Z.** (2019). Defect luminescence and its mediated physical properties in ZnO. *Journal of Luminescence*, 208, 225-237. doi: 10.1016/j.jlumin.2018.12.050

[113] **Biby, A. H., Tolba, S. A., & Allam, N. K. (2021).** Unveiling the role of carbon defects in the exceptional narrowing of m-ZrO2 wide-bandgap for enhanced photoelectrochemical water splitting. *International Journal of Hydrogen Energy*, 46(41), 21499-21511. doi: 10.1016/j.ijhydene.2021.03.248

[114] **Mueller, F., Gutsche, A., Nirschl, H., Geiger, D., Kaiser, U., Bresser, D., & Passerini, S.** (2016). Iron-doped ZnO for lithium-ion anodes: impact of the dopant ratio and carbon coating content. *Journal of The Electrochemical Society*, 164(1), A6123. doi: 10.1149/2.0171701jes

[115] **Wang, X., Wang, Y., Wu, M., Fang, R., Yang, X., & Wang, D. W.** (2022). Ultrasonication-assisted fabrication of porous ZnO@ C nanoplates for lithium-ion batteries. *Microstructures*, 2(3), 2022016. doi: 10.20517/microstructures.2022.11

[116] **Thauer, E., Zakharova, G. S., Andreikov, E. I., Adam, V., Wegener, S. A., Nölke, J. H., ... & Klingeler, R.** (2021). Novel synthesis and electrochemical investigations of ZnO/C composites for lithium-ion batteries. *Journal of Materials Science*, 56(23), 13227-13242. doi: 10.1007/s10853-021-06125-4

[117] **Shen, S., Zhong, W., Huang, X., Lin, Y., & Wang, T.** (2019). Ordered ZnO/Ni hollow microsphere arrays as anode materials for lithium ion batteries. *Materials*, 12(7), 1193. doi: 10.3390/ma12071193

[118] **Lai, Y., Liu, W., Fang, J., Qin, F., Wang, M., Yu, F., & Zhang, K.** (2015). Fe-doped anatase TiO 2/carbon composite as an anode with superior reversible capacity for lithium storage. *RSC advances*, 5(114), 93676-93683. doi: 10.1039/C5RA19518G

[119] **Zhang, G., Zhang, H., Zhang, X., Zeng, W., Su, Q., Du, G., & Duan, H.** (2015). Solid-solution-like ZnO/C composites as excellent anode materials for lithium ion batteries. *Electrochimica Acta*, 186, 165-173. doi: 10.1016/j.electacta.2015.10.133

[120] **Khairudin, A., Suhaimi, S., Mohd Taib, N. A., Mohamad Isa, M. I. N., & Wan Ismail, W. Z.** (2023). A review study of binary and ternary ZnO/C composites as anodes for high-capacity lithium-ion batteries. *Ionics*, 29(12), 4939-4969. doi: 10.1007/s11581-023-05241-2

[121] **Yang, Z., Shen, J., & Archer, L. A.** (2011). An in situ method of creating metal oxide–carbon composites and their application as anode materials for lithium-ion batteries. *Journal of Materials Chemistry*, 21(30), 11092-11097. doi: 10.1039/C1JM10902B

CURRICULUM VITAE

Name Surname **:** Orhun OĞUZ

EDUCATION **:**

- **B.Sc.** **:** 2021, Istanbul Technical University, Faculty of Chemical and Metallurgical Engineering, Metallurgical and Materials Engineering Department

PROFESSIONAL EXPERIENCE AND REWARDS:

- **Oğuz O.,** Berkman O., Gul Y.E., Gursoy A.S., Bayboğa E., Keleş Ö., Gürmen S., 2021: A Comparative Study of Comparison of Recycling Methods for Lithium Ion Batteries. 5th International Symposium on Materials for Energy Storage and Conversion. September 14-17. 2021 Virtual Meeting. Best Poster Award.
- Since 2022, Turkish Petroleum Refineries A.Ş. (TÜPRAŞ) R&D Department – Materials Researcher

PUBLICATIONS, PRESENTATIONS AND PATENTS ON THE THESIS:

- **Oğuz O.,** Karahan B.D., 2024: Valorization of Hot Dip Galvanizing Dross As Anode Active Material For LIBs. International Graduate Research Symposium. May 8-10. 2024 Istanbul. Turkey